Summer 2023

In-situ Thermal and Deformation Characterization of Additive Manufacturing Processes

Nicholas Phillips
Embry-Riddle Aeronautical University, phillin6@my.erau.edu

IN-SITU THERMAL AND DEFORMATION CHARACTERIZATION OF ADDITIVE MANUFACTURING PROCESSES

By

Nicholas Phillips

A Thesis Submitted to the Faculty of Embry-Riddle Aeronautical University

In Partial Fulfillment of the Requirements for the Degree of

Master of Science in Aerospace Engineering

June 2023

Embry-Riddle Aeronautical University

Daytona Beach, Florida

IN-SITU THERMAL AND DEFORMATION CHARACTERIZATION

OF ADDITIVE MANUFACTURING PROCESSES

By

Nicholas Phillips

This Thesis was prepared under the direction of the candidate's Thesis Committee Chair, Dr. Sirish Namilae, Department of Aerospace Engineering, and has been approved by the members of the Thesis Committee. It was submitted to the Office of the Senior Vice President for Academic Affairs and Provost, and was accepted in the partial fulfillment of the requirements for the Degree of Master of Science in Aerospace Engineering.

THESIS COMMITTEE

Sirish Namilae Digitally signed by Sirish Namilae Date: 2023.06.21 11:47:41 -04'00'

Chair, Dr. Sirish Namilae

Jeff Brown Digitally signed by Jeff Brown Date: 2023.06.21 12:52:08 -04'00'

Member, Dr. Jeff Brown

Yizhou Jiang Digitally signed by Yizhou Jiang Date: 2023.06.26 18:49:36 -04'00'

Member, Dr. Yizhou Jiang

Graduate Program Coordinator,
Dr. Daewon Kim

Date

Dean of the College of Engineering,
Dr. James W. Gregory

Date

Associate Provost of Academic Support,
Dr. Christopher Grant

Date

ACKNOWLEDGEMENTS

I received a great deal of support during my time working on this research. Firstly, I would like to thank my advisor, Dr. Sirish Namilae, whose expertise and experience helped me to even formulate and begin this research and provided me with constant support in developing the methodology and the necessary equipment required. I would like to thank Dr. Jeff Brown for providing me with the thermal camera used for the research and insightful feedback regarding the analysis of my thermal data. I would like to thank Dr. Yizhou Jiang, whose experience with the use of CCD cameras was useful in establishing the methodology for the deep neural network analysis.

I would also like to thank Martina Jani for teaching me how to perform the PLA analysis and providing insightful feedback when it came to translating the analysis to composite printing. I would like to thank Deepak Kumar for allowing me to utilize his zero-bias neural network for this research and providing feedback on my use of the network.

Finally, I would like to thank my close friends and family for providing me with the emotional support required to keep going throughout the whole endeavor.

ABSTRACT

Additive manufacturing (AM) is a rapidly growing industry with numerous applications in the aerospace industry such as aircraft parts and emergency tools on the International Space Station. Defects in additively manufactured structures, however, can waste a lot of time and money. Being able to monitor the manufacturing process for defects is one of the first steps which can be taken to mitigate these losses. This study focuses on the use of thermography in conjunction with deep learning to identify flaws during 3D printing of composite structures made using Onyx, a mixture of chopped carbon fiber and nylon, composite prints. In addition, polymeric structures using polylactic acid (PLA) were analyzed using thermography and digital image correlation (DIC) to understand the interactions between the thermal variations and resulting deformation.

The inclusion of a zero-bias deep neural network (ZBDNN) to classify given images can also show real-time monitoring of defects in composite prints as a realizable goal. The ZBDNN was trained to classify thermal images of undamaged prints based on which layer of the print they occurred on and to set aside any of these images containing defects. The addition of a non-bias layer in the deep neural network ensures the classifications of these images remain consistent and accurate, with a learning accuracy of over 90%. The algorithm was also used to analyze grayscale images from multiple angles of the prints and compared these images to thermal images as another means of detecting defects in each print. The use of these multiple data sources may be used as the basis for an early-warning detection system for real-time analysis.

TABLE OF CONTENTS

LIST OF FIGURES

NOMENCLATURE

AM	Additive Manufacturing
PLA	Polylactic Acid
DIC	Digital Image Correlation
DNN	Deep Neural Network
ZBDNN	Zero-Bias Deep Neural Network
ASTM	American Society of Testing and Materials
SM	Subtractive Manufacturing
ABS	Acrylonitrile Butadiene Styrene
FDM	Fused Deposition Modelling
CCD	Charge-Couple Device
CAD	Computer-Aided Design
EFF	Extrusion Free Form
NASA	National Aeronautics and Space Administration
FEA	Finite Element Analysis
CFRP	Carbon Fiber Reinforced Polymer
NDE	Non-Destructive Evaluation
PID	Proportional–Integral–Derivative

1. Introduction

In this chapter, the problem this research attempts to address is introduced alongside the importance and limitations of additively manufactured composites in the aerospace industry. Additionally, the motivation for the research and the objectives of this study are discussed.

1.1 Additive Manufacturing of Composites

Committee F42 of the American Society of Testing and Materials (ASTM) defines additive manufacturing (AM) as a "general term for those technologies that successively join material to create physical objects as specified by 3D model data" [1]. AM is finding increasing use in multiple industries with the aerospace industry being one of the major consumers of AM technology. An analysis from HUBS reveals the net worth of the AM industry is projected to double in 2026 from 2023 as seen in Figure 1.1 [2].

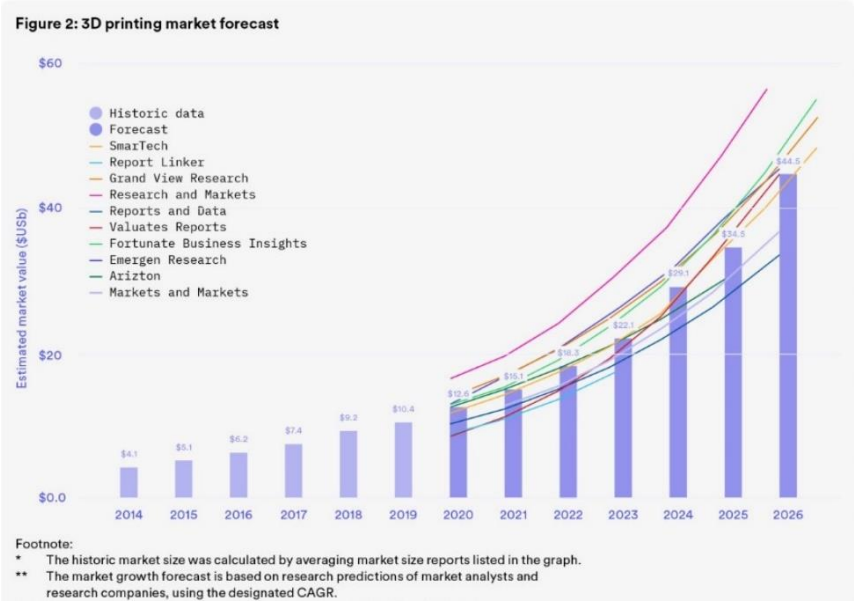

Figure 1.1 Projected market value of the additive manufacturing industry [2]

AM can be very appealing for many companies due to its prototyping ease and efficiency. Parts manufactured using AM technologies allow for multiple copies of a part to be produced at once to speed up testing times. These parts can also be made with geometries and tolerances that would be expensive, difficult, or impossible through traditional subtractive manufacturing (SM) means. AM parts also have very little waste material, with waste usually only every coming from printed supports to stabilize a part during printing.

AM however has the downsides of being slower and more expensive than traditional SM methods. Due to the nature of how most AM methods function, the desired materials must be purchased in a spool or powdered format, which presents a higher upfront cost for materials. Due to how parts are assembled in AM processes, it can often take longer to produce a more generic part than a SM process would take to produce the exact same part.

There are a wide variety of materials which are compatible with AM methods including plastics, metals, ceramics and composite materials. The most common materials used in AM are polylactic acid (PLA) plastic and acrylonitrile butadiene styrene (ABS) plastic since they are low-cost, widely available, and easy to use. Other materials which are frequently used in AM include titanium, aluminum, Inconel, stainless steel, and carbon fiber. This research primarily focuses on PLA and Onyx. Onyx is a trademarked composite material developed by Markforged. It is a mixture of chopped carbon fiber and nylon matrix in the form a continuous fiber filament.

There are multiple methods of developing parts using AM. One of the most common being fused deposition modelling (FDM). This method uses a spool of the desired material is fed through a heated nozzle and deposited onto a print bed, working one layer at a time. The printers used in this research utilized the FDM method of printing. Other common methods of printing include binder jetting, which distributes a powdered version of the desired material and applied a binder

to adhere the powder together one layer at a time, and powder bed diffusion, which uses a laser to melt the powdered material together layer by layer.

1.2 Motivation for this Research

Motivation for this research stems from frequent occurrence of defects during additive manufacturing. These defects can cost large amounts of time and money if they are not caught quickly. Common defects which can occur during FDM printing include voids, warping, poor adhesion, over-extrusion, and bed obstructions. Some of these defects are shown in Figure 1.2 Processing induced defects during printing can lead to further defects when the structures are used, premature failure during use, or complete failure of the printing of the structure. This is particularly impactful on strcutures which cannot be manufactured through traditional subtractive manufacturing methods due to either their design or the choice of the material.

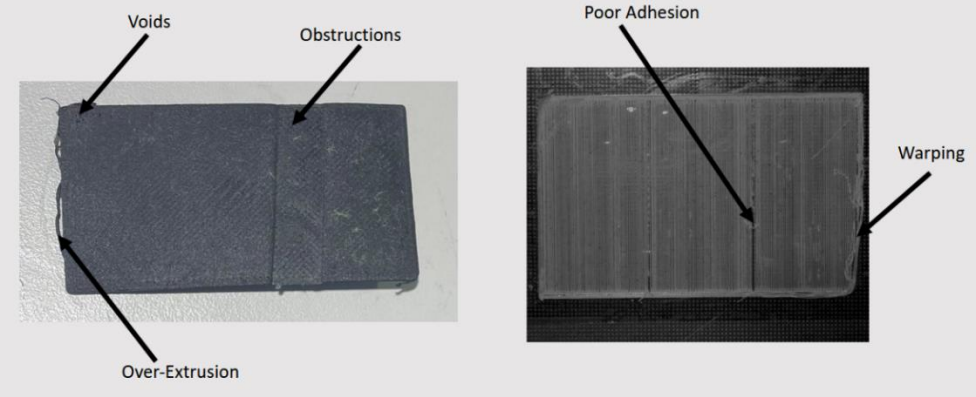

Figure 1.2 Examples of defects captured during testing

Developing a system for early detection of defects in prints is one the first step to reduce the occurancce of defects and improve the quality of printed parts. These defects stem from a number of potential sources. Improper print settings is a common cause for printing defects. These settings

include nozzle and bed temperatures, layer thickness, print rate, slicing direction, improper or lack of support structures, and many more. Other sources for defects include too much moisture in the printer or printing material, unclean or uneven print bed, defects or wearing of printer components, and improper ventilation in the printer.

It is possible to measure parameters impacted by defect occurances, such as thermal expansion and cooling patterns, to determine the quality of the print. Digital Image Correlation (DIC) cameras, grayscale charged-couple device (CCD) camera, and thermal imaging cameras are common methods of insitu data collection of print characterisitics performed by prior research. Despite the use of methods seen in other publications, the methodology and analysis methods are unique to this research.

A deep neural network (DNN) was incorporated to further analyze the data from the thermal and CCD cameras. DNNs are learning algorithms which can identify patterns from a training set of images nad use the data from the training images to classify new images based on how closely the new data matches the training data. The DNN used in this research would sort the images by which layer the image is of. If a defect was detected in a given image, it would be given its own classification. When plotting the results from the DNN analysis in a Voronoi diagram, the images would be clustered in groups by their class, with defects being placed near the cluster that most closely matches which layer the defect occurred on.

1.3 Objectives

This research employs combinations of thermography, DIC, and greyscale imaging to provide real-time analysis of the characteristics of additively manufactured parts using the FDM process. The measured characteristics are used to form correlations with the occurrence of defects in printed parts. Employing computational methods of analyzing the characteristics of printed parts can validate the correlations between print characteristics and defect occurrences.

The objectives of this research are:

1. Develop in-situ monitoring methods for the FDM process of composite materials.
2. Correlate measured process parameters with the occerance of defects.
3. Utilize deep neural networks to classify image data based on layer and defect presence
4. Combine multiple data sources into a single DNN analysis

2. Review of the Relevant Literature

This chapter provides details regarding the background literature relevant to this research. Previous studies on the testing methods, equipment and materials relevant to current study are discussed.

2.1 Additive Manufacturing

There are different methods of additive manufacturing, but all methods involve some common steps for part creation. The process typically begins with the development of a computer-aided design (CAD) model of the desired part. The CAD part can be created using software such Solidworks or AutoCAD. The designed part can then be converted into a compatible file type, typically .STL, which is processed further using slicer programs, which establishes the printing parameters for a specific 3D printer model. This slicer program dictates the printing direction, any supports for the part during printing, layer thickness, etc. From there, the part can be printed then post-processed with methods such as sintering or acid baths to remove the supports.

The printing process used for this research was the fused deposition modelling (FDM) process, also called the Extrusion Free Forming (EFF) method. The FDM process is the most common method of AM due to being a rapid and inexpensive process which can produce parts of a wide range of sizes. This method consists of a coil of filament run through a heated printing nozzle which deposits the softened material onto a printing bed where it immediately begins hardening [3]. A breakdown of the common commercial AM processes is outlined in Figured 2.1.

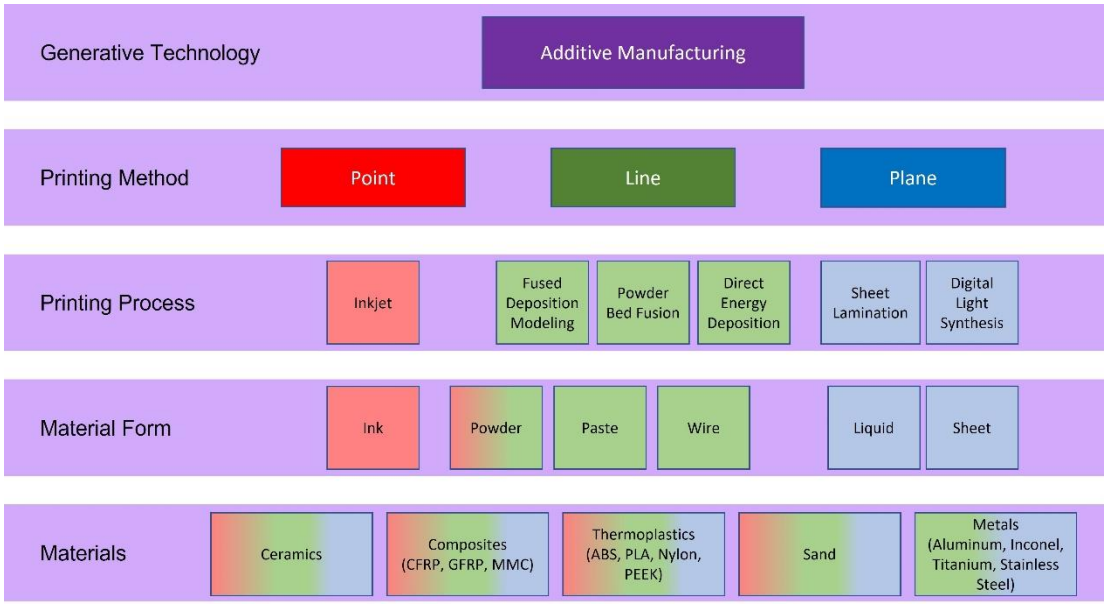

Figure 2.1 Classifications of AM methods

Additive manufacturing has found uses in multiple industries with engineering fields such as automobile and aerospace being among the top consumers of AM technology [4]. Parts produced using AM can benefit from a reduction in production time and cost along with lighter parts and fewer total parts by combining multiple parts into single complex shapes not normally possible with traditional SM methods [5]. Within the aerospace industry, NASA has been using additive manufacturing for the development of research equipment such as the heat exchangers on Perseverance rover [6], and for full-scale rocket components such as the nozzles manufactured using SLS shown in Figure 2.3 [7]. GE also uses AM technology to produce aircraft parts such as fuel nozzles and titanium fittings for the Boeing 787 [8].

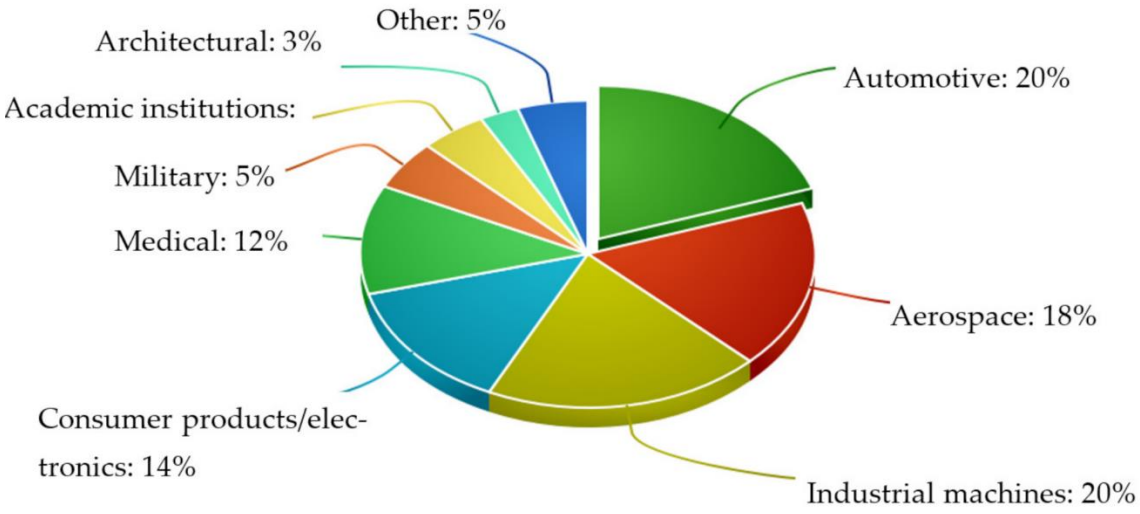

Figure 2.2 Breakdown of top consumers of AM technologies [4]

Figure 2.3 Prototypes of NASA's AM rocket nozzle [7]

2.1.1 Defect Formation and Impacts

Processing induced defects in AM structures can completely ruin a print before it even finishes printing. Defects can occur at any point in the 3D printing process due to any aspect of the printer, printing process, or part geometry. The printing speed, the part thickness, the line

spacing, overhangs, and even the size of a part can contribute to the formation of defects in a part [9]. Defects that can occur in AM parts include voids, dislocations, surface roughness, delamination, and residual stresses. The nature of these defects can result in parts which have fatigue life half as long as the same parts produced through traditional SM methods [10].

Karpenko et al. [11] discuss how residual stresses in AM structures affect fatigue crack growth. The team uses a numerical model, a continuum model, and a finite element model to analyze a titanium plate made with AM. The main cause of residual stresses in AM structures is because AM structures are made in layers which makes the structure anisotropic. These two areas are the main aspects of the calculations used here and assume the plate is under thermal-mechanical cyclic loading. The study shows that tensile stresses are likely to accelerate crack growth in AM structures and residual compressive stresses mitigate the growth of cracks. It was also found that higher temperatures increase the rate cracks grow at. The effects of the residual stresses were shown to be accurately predicted through finite element analysis (FEA) and manual calculations. Being able to properly predict how stresses form in the structure can help improve current printing methods to help mitigate the formation of residual stresses in AM structures.

Fernandes et al. [12] discusses the mechanical properties of AM composites. The air voids can cause discontinuities which can hamper the performance of the composite. The team used continuous carbon fiber reinforced polymer (CFRP) composites printed using FDM for testing the tensile strength, shear strength, and dynamic strength of printed composites. The tests were also run using unidirectional samples with 0°, 45°, 90°, and concentric alignments. The dynamic testing was done with a test at static vibration at 1 Hz with a temperature sweep from 30℃ to 160℃, a test at a constant temperature of 30℃ with a frequency sweep from 1 Hz to 100 Hz, and a test sweeping both temperature and frequency.

The shear testing showed the samples had an average interlaminar shear strength of about 31 MPa. The failure of the samples occurred due to delamination which is more likely to occur in AM composites due to being produced at a lower pressure than traditional composites. The tensile test showed the samples had an average shear strength of about 500 MPa with failure occurring in the fibers likely due to discontinuities during the printing process.

2.2 AM Materials

This section details the materials analyzed in this research. Polylactic acid was used as a base reference material while the composite material was the primary focus.

2.2.1 Polylactic Acid

Polylactic Acid (PLA) is one of the most widely used materials for AM parts, especially with FDM. It is a thermoplastic polyester with a chemical formula of $(C_3H_4O_2)_n$. PLA was used in this research as a control material to establish a baseline comparison for other materials. PLA is typically used for its low melting temperature (170-180°C), high print rate, ability to consistently create sharp corners and edges, and minimum required post-processing [13]. The material properties for PLA include a tensile strength, elastic modulus, shear modulus, yield strength and Young's modulus of 59 MPa, 3500 MPa, 1287 MPa, 70 MPa, and 1280 MPa respectively [14].

2.2.2 Carbon Fiber Composites

Composite materials consist of a bundle of fibers, typically glass, carbon, or natural materials, surrounded by a matrix material, typically a resin polymer. Composites are one of the newer materials to be used in AM which opens more options for replacing common materials used in the production of commercial products. A popular example of this being Boeing's 787 Dreamliner which is 50% composites, shown in Figure 2.4, as opposed to the previous 777 which is only 12% composites [15]. The composite used in this research, called Onyx, is made up of carbon fibers in

a nylon matrix. The material properties for Onyx include a tensile modulus, tensile strain, and flexural modulus of 2.4 GPa, 25%, and 3.0 GPa respectively [16].

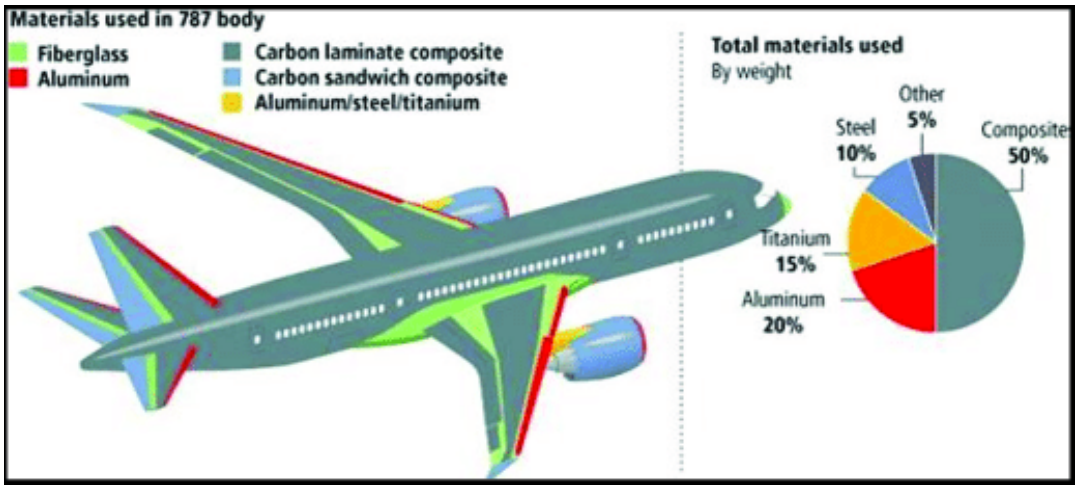

Figure 2.4 Mapping of materials used in the Boeing 787 [15]

In all the tests of various layups performed by Fernandes et al., the concentric fiber alignment performed the best, which shows an interesting use case for AM composites given this alignment method would be difficult to produce with traditional composite manufacturing [12].

2.3 In-situ Methods

This section covers the background on thermography and digital image correlation (DIC) and how they are used in analyzing parts produced with AM.

2.3.1 Thermography

Thermography is a non-contact method of non-destructive evaluation (NDE) which can be used to detect defects through the appearance of thermal patterns in the measured structure [17]. Thermal cameras used for thermography show the temperature differences between different sections of an observed part by measuring the infrared radiation emitted by the part. Thermography

can also be used for an initial observation to determine if more detailed analysis is required to determine the exact location and type of damage present in a part.

Wilson et al. [18] compared the performance of thermal imaging cameras to that of direct contact sensors using a proportional–integral–derivative (PID) controller. The experiment was performed on a scaled version of an injection mold system with controllable temperature zones. Thermocouples were installed at each point and a thermal camera was pointed at the entire system. The thermocouples controller measured the temperature at the individual zones while the camera analyzed the entire structure, with a PID controller for both measurement systems. The experiment was run using a digital model for simulation and a physical experiment to verify the results for accuracy. The results of the physical experiment showed that the thermal camera system had nearly identical reading to that of the simulation predicted values with the same response time. The thermocouple was shown to be slightly less accurate than the camera system and was less sensitive to changes in temperature.

Borish et al. [19] makes use of thermal cameras and other methods to determine thermal stresses which appear in a single layer of an AM structure. The combination of low creation time and high heat can result in flaws occurring in a layer of an AM structure. The team modified the printer they were using to allow support of a moving thermal camera to capture the layers as they were being printed. The testing was done on a spiralized cube and a podium stand which were to be printed using carbon fiber reinforced acrylonitrile.

In the case of the cube, it was found that the material was too hot to be able to hold such a shape and resulted in failure mid-printing with each layer being performed in 10-12 seconds. With a longer print time, the cube was able to support its own weight as the layers were allowed to cool. The podium not only needed the extra time to cool, but also had excess material due to temperature

differences between the layer and the plastic being printed not allowing proper bonding. This experiment shows that temperature and time need to be adequately adjusted prior to printing to avoid structural failure and waste, however it is difficult to know how to adjust these factors ahead of time.

2.3.2 Digital Image Correlation

Digital Image Correlation (DIC) is an NDE technique which allows for the measurement of changes between 2D and 3D images to determine the deformation and strain occurring in a particular part or structure over time [20]. Typically, a natural or painted speckled pattern is used for the algorithm to track the changes. This process is visualized in Figure 2.4. This method can easily be performed in tandem with other analysis methods, such as thermography, to determine correlations between mechanical behavior and damage occurrences.

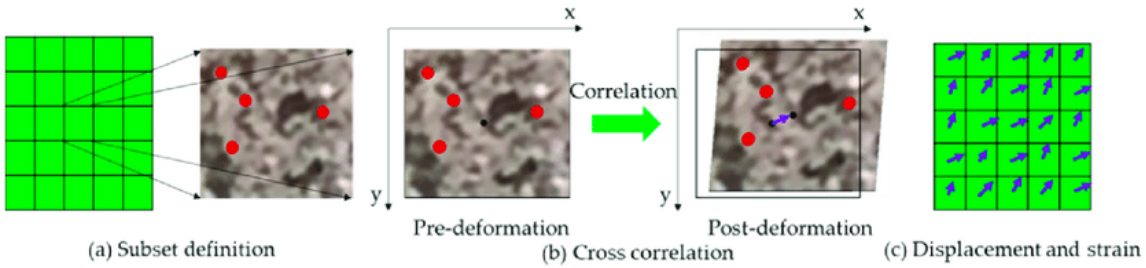

Figure 2.5 Diagram of DIC analysis [20]

Spencer et al. [21] used digital image correlation (DIC) to monitor residual thermal stresses in composites made using additive manufacturing. The DIC camera system was used to measure linear translation of natural speckles found in the printed surface over time. This experiment was applied to both a small-scale and large-scale (up to 100 layers) product. The measurements of the DIC camera were within 3.57% of the actual displacements of the speckle pattern. It was found

the maximum displacement occurred along the walls of the structure, with 4.20mm in the horizontal and 6.06mm in the vertical direction. The least displacement was measured at the center of the structure at 2.06mm and 1.24mm in the horizontal and vertical directions respectively. It was also found that more layers exaggerated the warpage in the part up until around 50 layers where displacement plateaued.

2.4 Computational Methods

This section covers how deep neural networks function and how they are used to validate the results of the in-situ testing methods.

2.4.1 Deep Neural Network

Deep neural networks (DNNs) are a type of machine learning based on how neurons in the brain send signals to one another [22]. They are comprised of an input layer, at least one hidden layer, and an output layer, where the output of one layer is the input of another layer, visualized in Figure 2.6 [23]. The neurons within a layer have thresholds which trigger the activation of data transference from that neuron to the neurons of the next layer. DNNs can significantly reduce the amount of time required to classify data, such as image classification. However, like all machine learning algorithms, training data is required for DNNs to function accurately. DNNs also typically incorporate biases to speed up the analysis, but this bias can result in misclassifications and missing data [24].

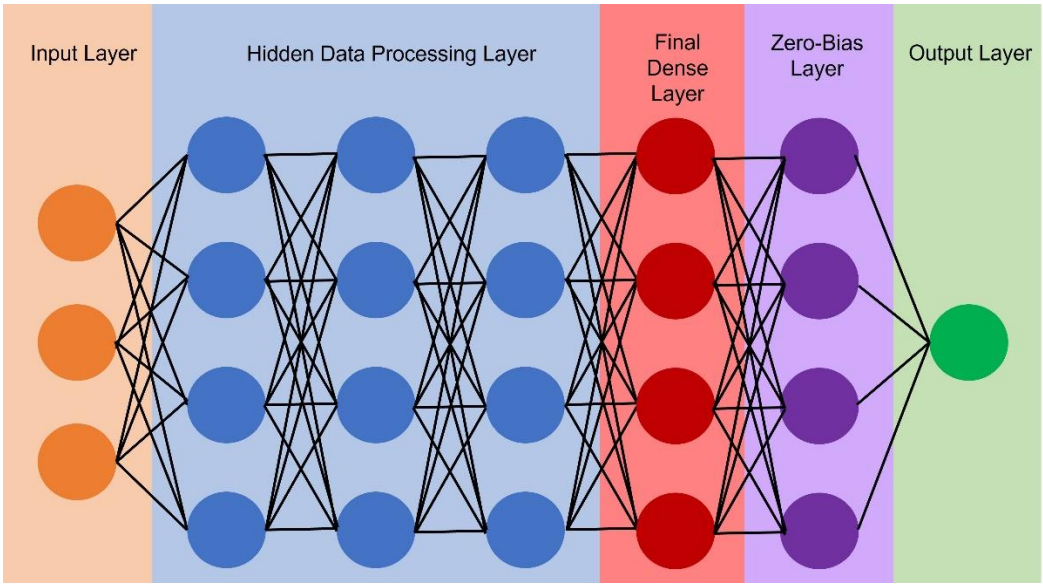

Figure 2.6 Deep neural network layer diagram

The Blackbox nature of typical DNNs means that these learning algorithms can develop biases during the training process. These biases can lead to the misidentification of defect occurrences in the processed training images that can carry over into non-training images. To correct the formation of bias in the training of the DNN, a zero-bias layer is inserted just before the output layer. This non-bias layer allows for not only correctly identifying if the image is abnormal or not, but also provides a "what if" classification that states where the image would have been classified if not identified as abnormal. It has also been shown that the inclusion of a zero-bias layer results in a more uniform distribution of classes which can lead to better identification of abnormalities in a dataset, with most errors occurring from overlapping data clusters [25][26].

2.5 Summary

The current research in the field of additive manufacturing shows that it has great potential for the future of aerospace production, however the defect occurrences must be mitigated for AM to see further improvement and development. Identifying how these defects occur in various printing

methods and materials is the first step to mitigate the formation of defects in the future. The use of thermography and DIC in previous research has shown promising results in the identification of defects and determining why the defects occur. Utilizing machine learning in the form of a DNN can help speed up and further confirm the results collected from the in-situ monitoring methods.

3. Experimental Methods

3.1 In-situ Characterization Methodology

The in-situ procedure for the monitoring of defects in additively manufactured composites is divided into 6 main steps:

1. Creating a setup consisting of the PLA printer, thermal camera, and DIC camera.
2. Capturing the changes in temperature and strain in the PLA over time.
3. Developing relations between the strain and temperature data.
4. Use knowledge obtained from PLA testing to develop an Onyx testing method.
5. Capture images of the Onyx material with the thermal camera and CCD camera.
6. Process temperature data collected from the Onyx testing.

3.2 Materials, Equipment, and Software

This section provides details on the materials and equipment used in this research. Experimental details and specifications are also provided in this section. Software associated with equipment is also described in this section.

3.2.1 Marble PLA

PLA was used for early data collection for two main reasons. The first being PLA is the most common material to use for additive manufacturing, so it is easy to 3D print to develop new procedures. The second reason being E-notepad produces a marble style PLA which is a primarily white color with black speckles randomly spread throughout the material. This random spread of speckles would be able to provide accurate readings for the DIC analysis without needing to develop a method of incorporating the pattern manually.

Figure 3.1 A spool of marble-style PLA

3.2.2 Onyx

The Onyx material produced by Markforged was selected as the composite material for analysis in this research. The MicaPlex next to Embry-Riddle's Daytona campus was already in possession of the Mark Two printer produced by Markforged, so using the printer and associated materials would be the most convenient and cost-effective for analysis. The Onyx material consists of a nylon matrix infused with chopped carbon fiber pieces. Using a pre-made composite material would help with the cost-effectiveness and consistency of testing the composite.

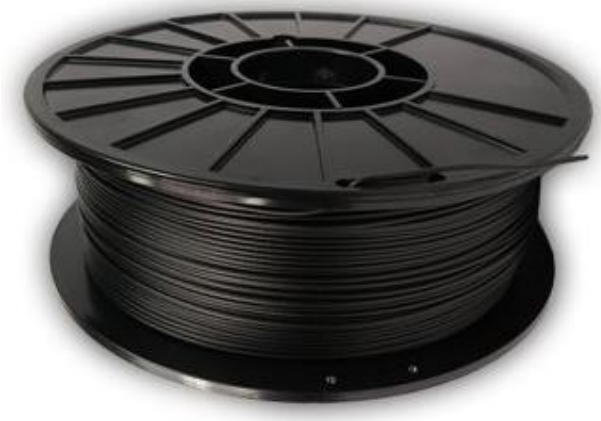

Figure 3.2 A spool of the Onyx material

3.2.3 Creality Ender 5 Plus

The Ender 5 Plus is an open frame style FDM 3D printer which enables easy viewing for the thermal and DIC cameras and allows both cameras to be used simultaneously. The maximum print size the printer allows for is 350mm x 350mm x 400mm with a precision level of +/-0.1mm. The inclusion of the BL Touch, filament sensor, and dual z-axes ensures consistency between tests.

The associated Creality slicer program was used to convert CAD data into G-code to guide the printer in the production of parts by controlling the layer thickness, nozzle and bed temperatures, printing speed, and pause timers.

Figure 3.3 The Ender 5 Plus 3D printer

3.2.4 Markforged Mark Two

The Mark Two is a closed-frame FDM printer that restricts camera access to the inside of the printer. The top and front panels of the printer do open, which allows for limited viewing of the print inside the printer. The maximum print size allowed by the printer is 320mm x 132mm x 154mm with a precision of +/-0.01mm. The Mark Two self-monitors all its internal components for performance degradation ensuring consistency between tests. The Mark Two also has a dry storage container for a material spool to mitigate ambient moisture entering the material.

The associated Eiger slicer program was used to import the CAD data and establish printing parameters. Being a proprietary program, the freedom to edit the G-code is limited, but open enough to allow for similar testing parameters to the PLA material. The main difference is the plate had to be reduced to a third of the size since the Eiger software does not allow for automatic pausing of a print mid-layer, so the part width was adjusted to match the point where the Ender 5 Plus would normally pause.

Figure 3.4 The Mark Two (right) beside the dry storage container (left)

3.2.5 DIC Camera and Software

A 2D DIC camera from Correlated Solutions was used to measure the strain in the printed plates. The camera has an in-plane resolution of 0.00002*Field of View and a strain measurement range of 0.010% to 2000%. The VIC-Snap software included with the camera was used to record the monochromatic images and the VIC-2D software was used to run the analysis on the captured images. The 2D version was opted for as it required no calibration, and the produced images would be easily compared to the thermal images captured at a similar angle. A starting point and image had to be designated for the software to be able to analyze the strain changes over time. A corrective equation (discussed later) was used to account for the increase in plate height during printing.

Figure 3.5 The DIC camera with attached lens

3.2.6 Thermal Camera and Software

The FLIR A655sc thermal camera was used to capture thermal data of additively manufactured plates during printing in real time. This camera has a resolution of 640x480 with a measurable temperature range from -40°C to 650°C within +/-2% of the true temperature. The Research IR software by FLIR was used for capturing videos and converting them into MATLAB files for post-processing.

Figure 3.6 The FLIR A655sc

3.2.7 CCD Cameras and Software

The FLIR Blackfly S CCD camera was used to capture pictures of the printed Onyx plates at various angles. The additional angles are compared against the thermal images in the deep neural network algorithm. This camera has a resolution of 2048x1536 and uses c-mount lenses with fixed focal lengths of 16mm and 29.3mm. The SpinView software was used to capture images of the printed plates at the same rate as the thermal camera capture.

Figure 3.7 The FLIR Blackfly S

3.3 Experiment Setups

The nature of the two printers having different enclosures meant that different setups were required for each setup. Both setups are detailed in this section. The setup for the Ender 5 Plus was created to determine a correlation between the thermal and strain characteristics and how those characteristics relate to the formation of defects. Once this correlation was determined, the experimental setup for the Mark Two could be simplified to accommodate for the more restrictive enclosure.

3.3.1 Setup for PLA Printing

All the prints for the PLA plates were run with a layer thickness of 0.2mm, nozzle temperature of 195°C, bed temperature of 65°C, and print speed of 60mm/s. The setup included both the thermal camera and the DIC camera as the open enclosure of the printer allowed for multiple cameras to capture the print at once.

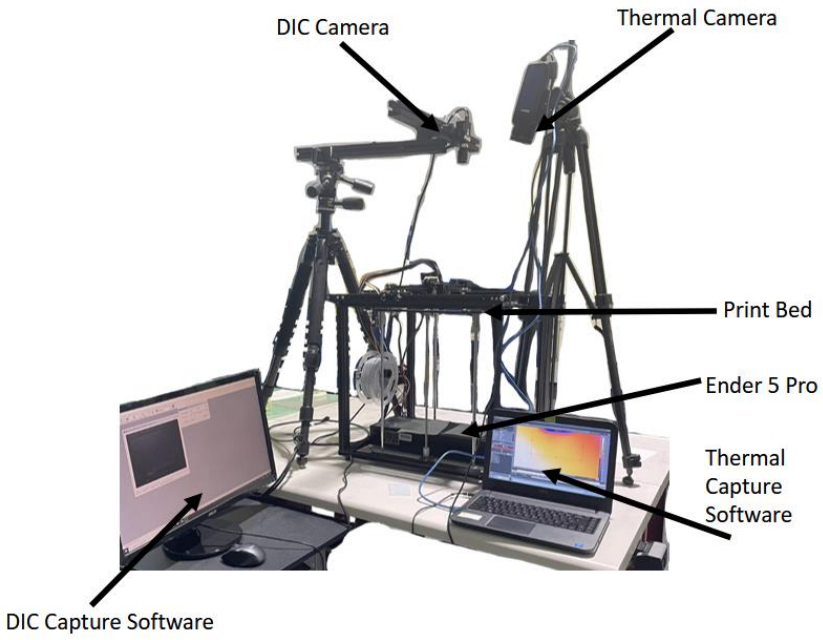

Figure 3.8 The experiment setup for the PLA material with labelled components

A printing pause was applied in the G-code at every third of a layer which would halt the printing and move the printer head out from above the printed plate to allow for 15 seconds of capture from the thermal and DIC cameras before the printer head returned to the part to resume printing. This was done to observe as much of the cooling process which occurs in a part as it is printed as possible, and the printer head would obstruct the view of the plate while it is printing.

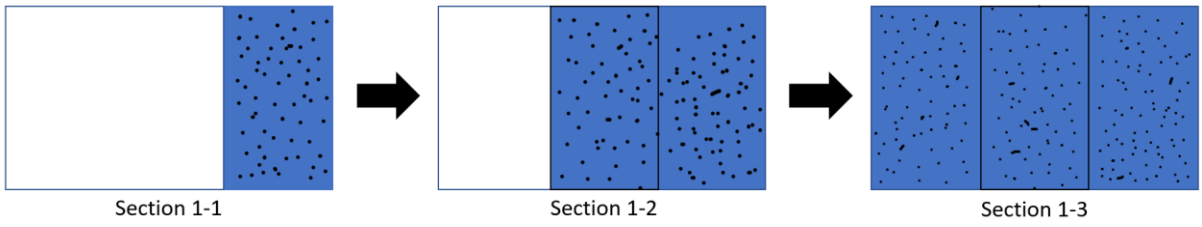

Figure 3.9 The printing procedure for the PLA tests

Defects in the PLA prints were introduced in a couple ways. The first method was to place thin material, such as packing tape or paper, on the bed that would make it harder for the plate to adhere. They were also introduced by using a pair of tweezers to pick and pry at the plate at various times to simulate different types of defects.

3.3.2 Setup for Onyx Printing

All the prints for the Onyx plates were run with a layer thickness of 0.2mm, nozzle temperature of 275°C, and print orientation of 45°/-45°/45°/-45°/45°. Only a thermal camera was used for this setup as the closed enclosure would restrict the amount of available space to view the part as it is printing.

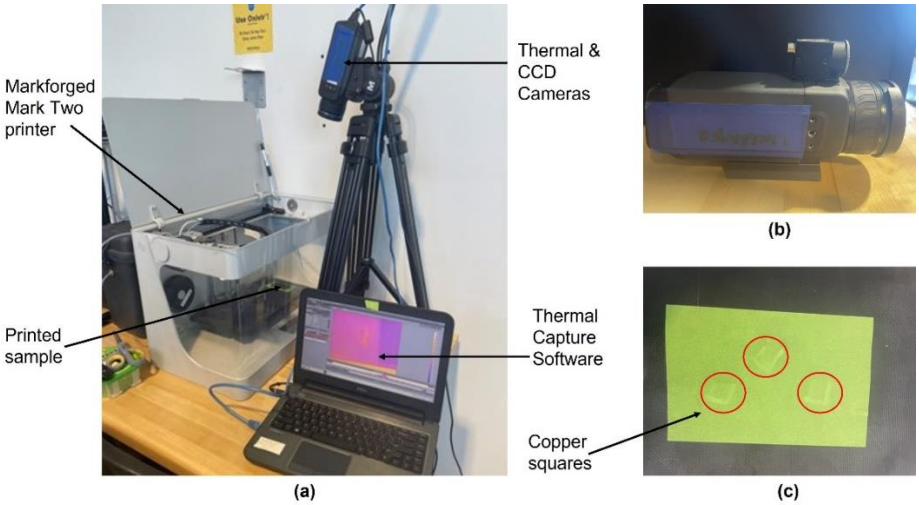

Figure 3.10 a) The labeled experiment components b) CCD mounting c) copper layout

A printing pause was applied at the end of each layer as pausing mid-layer was not an option within the Eiger program. To compromise, the plate size was reduced to be the size of one of the thirds from the PLA tests as to allow for the cameras to capture as much of the cooling process as possible.

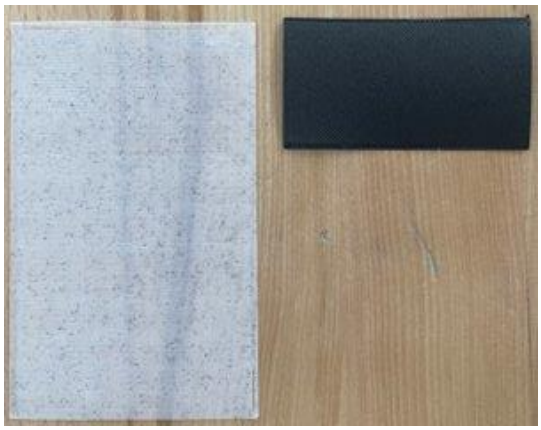

Figure 3.11 Comparison of the PLA (left) and the Onyx (right) prints

Defects for the Onyx testing were created by introducing thin copper squares taped to the print bed with painter's tape. The copper would serve two purposes. The first would be to create indents in the plate due to being a bed obstruction. The second would be to act as a heat sink to force uneven cooling in the part which could lead to further defects. Painters' tape was used since painters' tape can be used to help printed parts stick to the bed when poor adhesion is a concern.

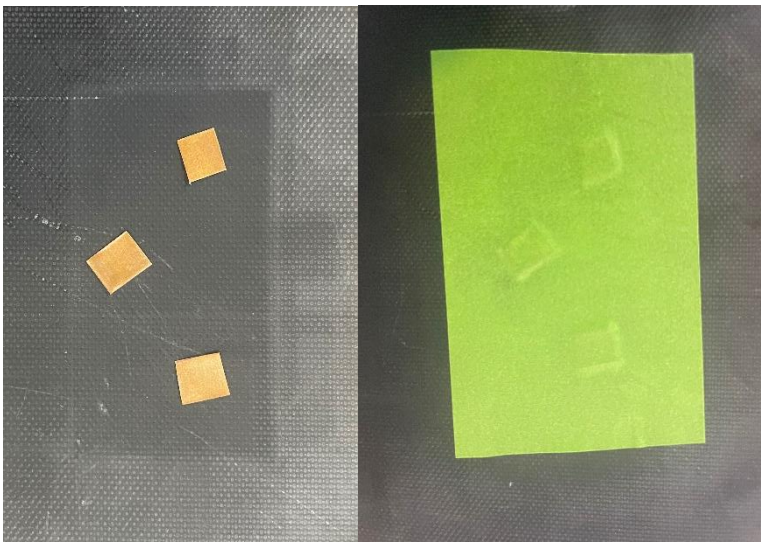

Figure 3.12 Copper squares on the print bed (left) and under the painters' tape (right)

3.3.3 2D DIC Correction

Whenever a new layer is added to the plates being printer, the additional layer changes the part in an axis not accounted for by a single camera. The print bed does shift in the opposite direction which can correct some of this displacement, but not all of it. This induces some error in the strain measurements.

It is possible for the errors produced this way to be accounted for after receiving the measurements. Jani demonstrated in her analysis of strain in additively manufactured plates using 2D DIC analysis that using a modified version of the pinhole equation can calculate the error in the strain measurements has a print changes layers, shown in equations 3.1 and 3.2 [27]. The strain error calculated using these equations can then be subtracted from the given strain by the software for the corresponding layer.

$$\Delta\varepsilon_{xx} = \frac{\partial U(\Delta Z)}{\partial x_s} \approx \frac{(\Delta Z)}{Z} \tag{3.1}$$

$$\Delta\varepsilon_{xx} = \frac{\partial U(\Delta Z)}{\partial x_s} \approx \frac{(\Delta Z)}{Z} \tag{3.2}$$

4. Deep Neural Network Modelling

Deep neural networks (DNN) models can learn intricate patterns from many structured picture datasets and can generate precise predictions based on training data. They are comprised of an input layer, at least one hidden layer, and an output layer, where the output of one layer is the input of another layer. The neurons within a layer have thresholds that trigger the activation of data transference from that neuron to the neurons of the next layer. DNNs can significantly reduce the amount of time required to classify data, such as image classification. However, these traditional methods require considerable model training, using both non-defected and defective data sets. This process limits their capabilities to detect the non-trained image data set and unknown images are forcefully classified into one of the known classes.

4.1 Zero-Bias Deep Neural Network

In this study, a novel method for transforming a standard deep neural network model into an abnormality detection model was utilized by adding zero bias layers. This approach enabled detection of untrained faults while using only non-defective data sets for training. The last dense layer was modified into two distinct layers—one standard dense layer and the other zero-bias layer. It should be noted that the addition of the zero-bias layer also increases the learning time for the algorithm and takes longer for the learning accuracy to increase due to a larger separation of fingerprints and less sensitivity to changing the spacing between fingerprints [28][29].

The zero-bias DNN model was initially trained using non-defective datasets and then the feature vector of known data sets from the zero-bias layer was extracted. The feature vectors of these known datasets are then utilized to calculate the centroid of each known class and a cutoff distance based on the Mahalanobis distance between the class-centered and furthermost feature vectors of each input data sample. If an input's Mahalanobis distance from the centroid of each class is more than the cutoff distance for all classes, it is considered as abnormal.

The ZBDNN used in this research was applied to AM by Deepak Kumar, a colleague of mine in the ERAU AE PhD program, who agreed to let me use and edit his code for the algorithm to fit the scope of this research.

```
rng(123)
tYfp = extractdata(squeeze(predict(dlnet, dlarray(cX(:,:,:,1:end),'SSCB'),...
    'Outputs','fc_bf_fp')))';
tY2fp = extractdata(squeeze(predict(dlnet, dlarray(uX(:,:,:,1:end),'SSCB'),...
        'Outputs','fc_bf_fp')))';
tYfp = tYfp./sqrt(sum(tYfp.^2,2));
tY2fp = tY2fp./sqrt(sum(tY2fp.^2,2));
tsnefp = tsne(gather([(dlnet.Layers(11).Weights);tYfp;tY2fp;classCenters]),...
    'Distance','correlation','NumDimensions',2,'Algorithm','exact');
%tsnefp = tsne([(dlnet.Layers(11).Weights);tYfp],'Distance','cosine');
set(0,'DefaultTextFontName','Times','DefaultTextFontSize',18,...
   'DefaultAxesFontName','Times','DefaultAxesFontSize',18,...
   'DefaultLineLineWidth',1,'DefaultLineMarkerSize',20)
sz = 100;
p = figure;
voronoi(double(tsnefp(1:size(dlnet.Layers(11).Weights,1),1)),...
    double(tsnefp(1:size(dlnet.Layers(11).Weights,1),2)))
%  voronoi(double(tsnefp(1:size(dlnet.Layers(15).Weights,1),1)),...
%     double(tsnefp(1:size(dlnet.Layers(15).Weights,1),2)))
hold on;
beginOftYFp = size(dlnet.Layers(11).Weights,1) + 1;
% plot(double(tsnefp(beginOftYFp:beginOftYFp+size(tYfp,1),1)),...
%     double(tsnefp(beginOftYFp:beginOftYFp+size(tYfp,1),2)),'g.')
gscatter(double(tsnefp(beginOftYFp:beginOftYFp+size(tYfp,1)-1,1)),...
    double(tsnefp(beginOftYFp:beginOftYFp+size(tYfp,1)-1,2)),...
    cY,[],[],30);
scatter(double(tsnefp(1:beginOftYFp-1,1)),...
    double(tsnefp(1:beginOftYFp-1,2)),sz,[0.6350 0.0780 0.1840],...
    'filled','DisplayName','Fingerprints','Marker','^');
%saveas(p, 'Normal_voronoi')

% scatter(double(tsnefp(end - size(tY2fp,1)+9:end-9,1)),...
%     double(tsnefp(end - size(tY2fp,1)+9:end-9,2)),sz,...
%     'DisplayName','Abnormalities','Marker','o');
scatter(double(tsnefp(225:end-9,1)),...
    double(tsnefp(225:end-9,2)),sz,'k',...
    'DisplayName','Abnormalities','Marker','o');
axis equal
```

Figure 4.1 MATLAB code for generating the Voronoi diagrams

```
[~,idx] = max(extractdata(dlnet.predict(dlarray(cX,'SSCB'))),[],1);
cond = (idx(:) == cY(:));
tYfp = extractdata(squeeze(predict(dlnet, dlarray(cX(:,:,:,1:end),'SSCB'),...
    'Outputs','fc_bf_fp')))';
tY2fp = extractdata(squeeze(predict(dlnet, dlarray(uX(:,:,:,1:end),'SSCB'),...
        'Outputs','fc_bf_fp')))';
tYfp = tYfp./sqrt(sum(tYfp.^2,2));
tY2fp = tY2fp./sqrt(sum(tY2fp.^2,2));
classCenters = [];
classMahalModels = {};
classMahalDistrib = {};
for i = 1:size(unique(Y),1)
    condOneClass = logical((cY(1:end) == i).*cond);
    oneClassFp = tYfp(condOneClass,:);
    avgOneClassFp = mean(oneClassFp);
    avgOneClassFp = avgOneClassFp./sqrt(sum(avgOneClassFp.^2,2));
    [C,m] = covmatrix(oneClassFp);
    classMahalModels{end+1} = {C,m};
    mahalDists = gather(mahalanobis(oneClassFp,classMahalModels{end}{1},classMahalModels{end}{2}));
    [~,den,xm,aClusterCDF]=kde(mahalDists,512,min(mahalDists),max(mahalDists));
    classMahalDistrib{end+1} = {xm,den,aClusterCDF};

%     centerDistDistrib = sum(oneClassFp.* avgOneClassFp,2);
%     filterCond = centerDistDistrib >= 0.3;
%     oneClassFp = oneClassFp(filterCond,:);
%     avgOneClassFp = mean(oneClassFp);
%     avgOneClassFp = avgOneClassFp./sqrt(sum(avgOneClassFp.^2,2));
    classCenters(end+1,:) = gather(avgOneClassFp);
end
cX = tmpCx;
cY = tmpCy;
```

Figure 4.2 MATLAB code for feature vectors for determining classes

4.2 Analysis using Deep Neural Network

The ZBDNN was trained using thermal images of the Onyx material. The classifications were given based on which layer was shown in the image. If an image was flagged as abnormal, containing defects in this case, then it would set the image aside. The image would be labelled as a defect and given an identifier of what label it would have gotten if not flagged as abnormal. This will allow not only verification of the occurrence of defects in the Onyx plates, but also identification of when and where the defects occurred. Due to limited available computing power, the training is only run over 60 iterations.

It is also possible to feed multiple images sources into a single analysis from the ZBDNN by treating the images of different sources as another set of classes. In this analysis, the thermal data was treated as classes 1-4 and the CCD data was treated as classes 5-8. It is important to note that the different inputs must be in the same format for the analysis to run as the matrix that reads color

values while be different sized depending on the format. This is why the thermal images were converted to grayscale prior to running the combined analysis.

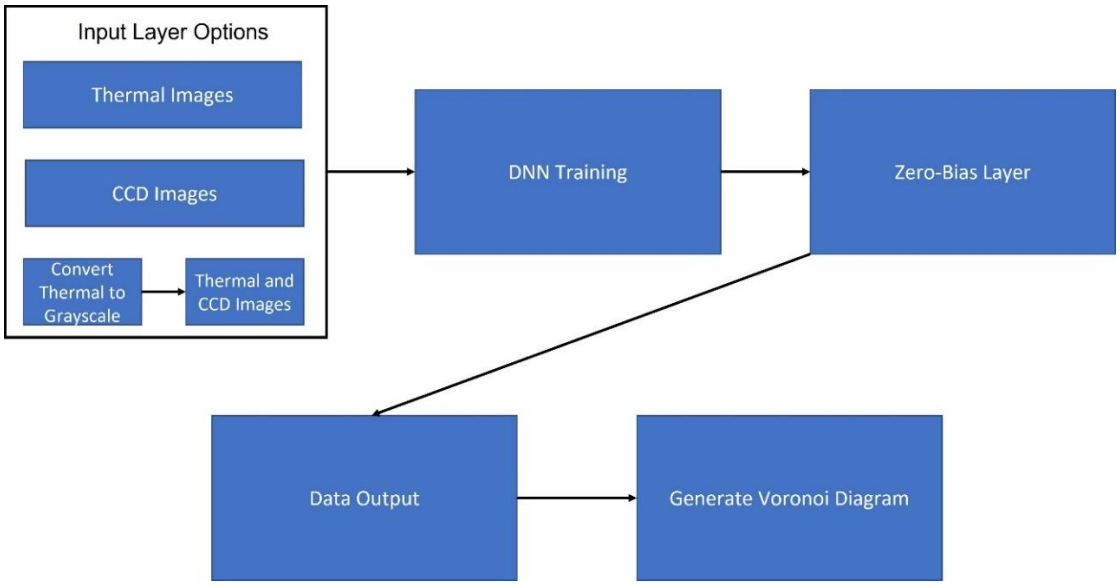

Figure 4.3 Flowchart detailing the DNN process

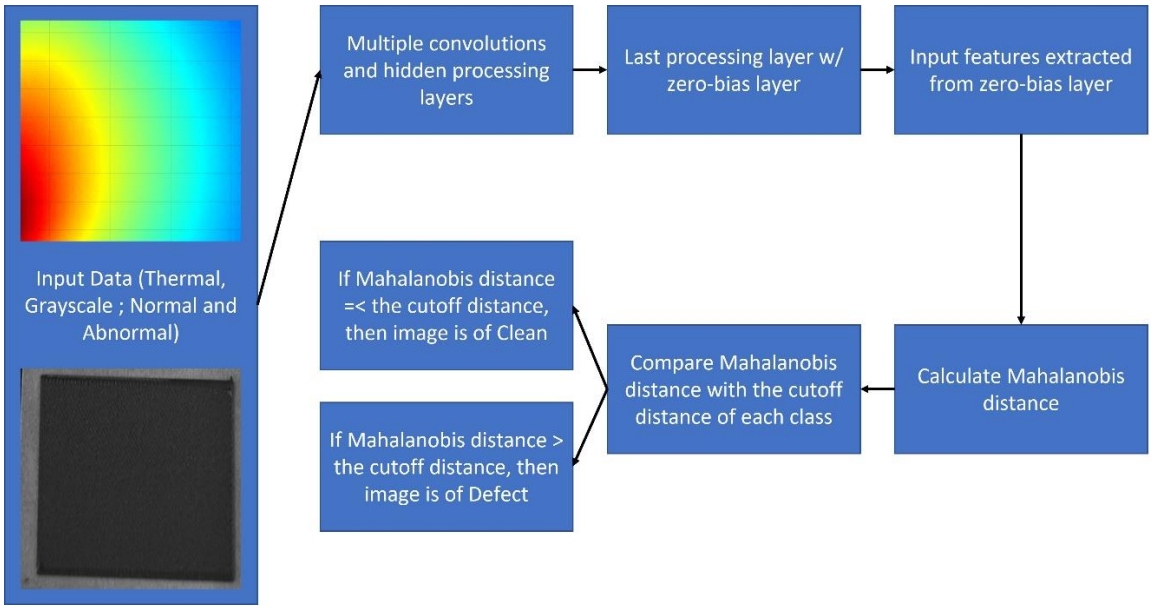

Figure 4.4 Flowchart detailing the DNN training

5. In-situ Characterization Results

This chapter details the results of the strain and temperature data collected from the tests of the PLA plates.

5.1 PLA Results

The data collected was post-processed through Excel and MATLAB. Naming of the sections follows the format of Section X-Y, where X corresponds to the layer and Y corresponds to the section of the layer. The strain data is discussed first, followed by the temperature data. The results of the strain and temperature are then compared to look for correlations between the two qualities. The data is then also compared to the occurrence of defects to determine correlations between the qualities and the formation of defects. All the plots and figures are from Section 2-2.

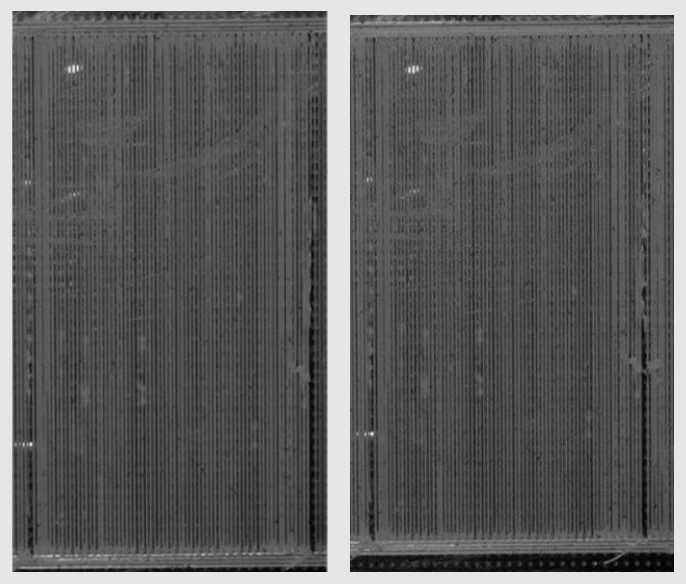

Figure 5.1 Sample sections for the clean PLA print (left) and the defective PLA print (right)

5.1.1 DIC Results

This section discusses the strain data in the PLA plates that was collected during the experiment. The clean prints are highlighted first, then the defective prints for comparison of the two test types.

5.1.1.1 Clean Prints

The strain in the xx-direction ranged from -0.00218 to 0.00830 while the strain in the yy-direction ranged from -0.00226 to 0.00132. The strains tended toward the lower half of the spectrum, with most of the extreme ranges around the edges of the section. The strains along the xx-direction had a roughly uniform pattern following the direction of the fibers while the yy-direction had a pattern perpendicular to the fibers. This uniformness indicates there are no defects imposing a change in the strain direction as the plate cools and shrinks. The strains are visualized in Figure 5.2.

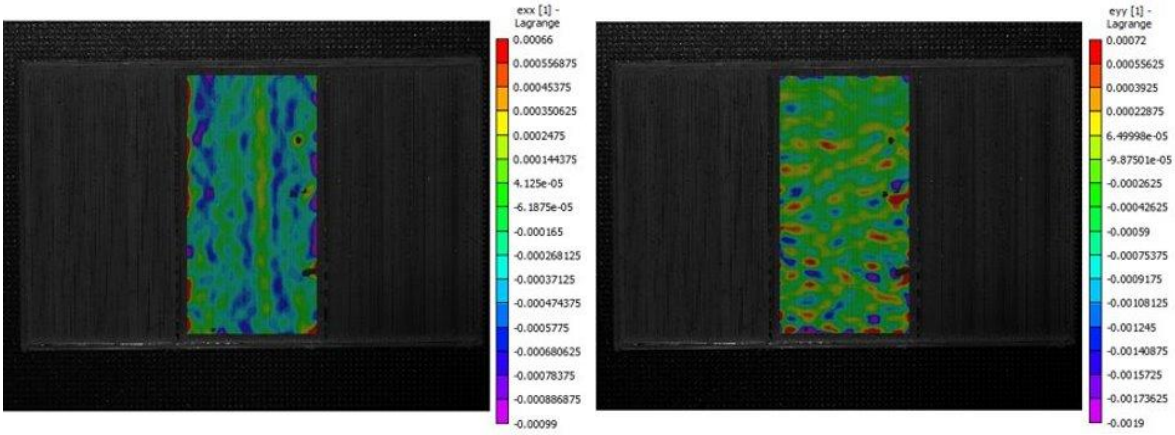

Figure 5.2 Strains in the xx-direction (left) and yy-direction (right) for the clean PLA prints

5.1.1.2 Defective Prints

The strain in the xx-direction ranged from -0.0075 to 0.00158 while the strain in the yy-direction ranged from -0.00354 to 0.00144. The strains tended towards the upper half of the spectrum, with the extreme ranges scattered throughout the plate. The strains along the yy-direction followed a similar pattern as the clean prints, however the strains along the xx-direction had a pattern towards the bottom left of the section. This pattern is indicative of defect occurrences either at the bottom of the section, or in the neighboring sections and impacting the observed section. These strains are visualized in Figure 5.3.

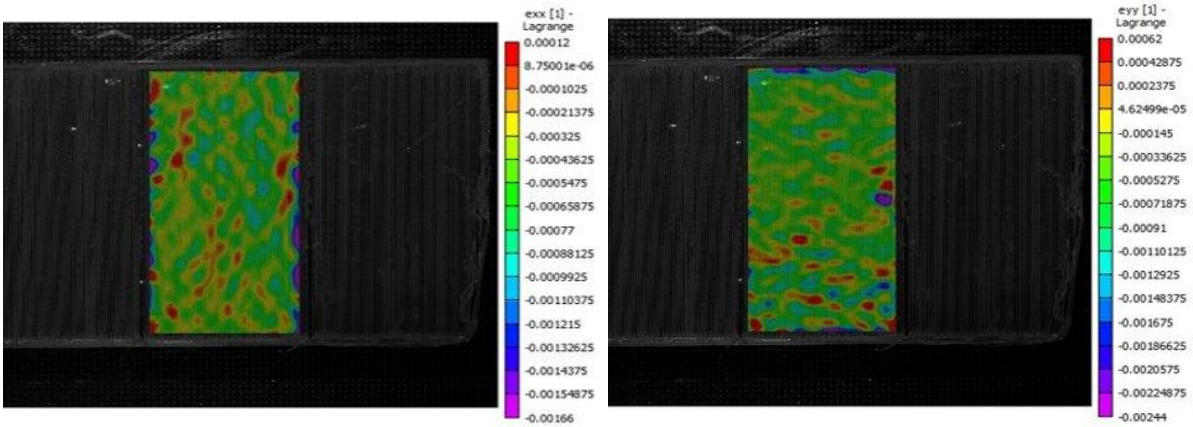

Figure 5.3 Strains in the xx-direction (left) and yy-direction (right) for the defect PLA prints

5.1.2 Thermal Results

This section discusses the thermal data in the PLA plates that was collected during the experiment. The clean prints are highlighted first, then the defective prints for comparison of the two test types. The strain tests indicate a defect in the plate, but the exact location cannot be determined with the strain test alone. The thermal tests can identify the exact location of the defect.

5.1.2.1 Clean Prints

The thermal mapping of the clean plate shows the most recently printed part of the plate as the hottest, being the right edge of section in this case, and the portion that's been left sitting the longest being the coldest, being the outer walls of the plate in this case. As there are no instances of defects in this print, there are no seemingly random occurrences of portions with a different temperature than the surrounding area. The thermal mapping is pictured in Figure 5.4.

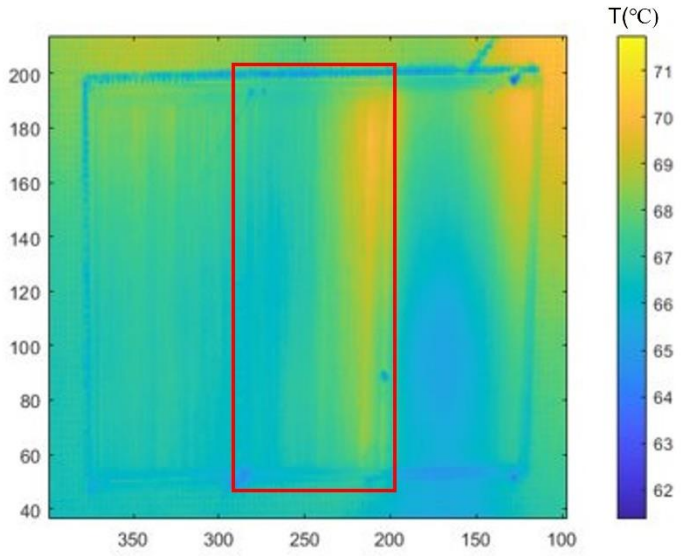

Figure 5.4 Thermal map of the clean PLA with the newly printed section boxed in

5.1.2.2 Defective Prints

The thermal mapping of the defective plate shows a similar pattern to the clean plate in the freshly printed section, except that the hottest section is noticeably larger than that of the clean print, which can be seen in Figure 5.5. This indicates there is some sort of pressure pushing along that edge of the section. There is no clear instance of a portion of this section being noticeably hotter or colder than the surrounding area, which means there is damage in a neighboring section

causing the increased size of the hit section. Looking at section 1-3, there is a band of much colder material around the lower outer edge, indicating that this part of the plate had not adhered to the bed properly and has started warping.

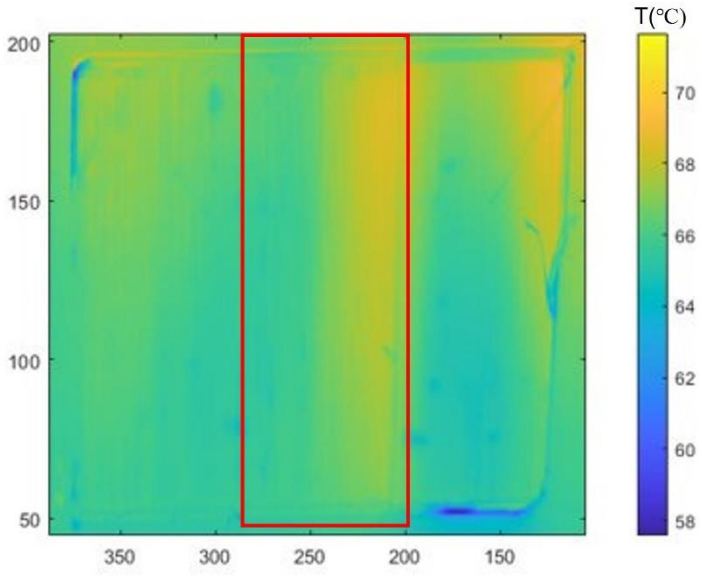

Figure 5.5 Thermal map of the defect PLA with the newly printed section boxed in

5.2 Relations between Thermal and Strain and the Formation of Defects

The average values of the temperature and the strains in the xx-direction and the yy-direction are plotted beside each other over time. The values of the clean print are in Figure 5.6 and the values of the defective prints are in Figure 5.7. The clean print has a temperature plot with clear steps whenever a new section of the plate is completed while the strain had small fluctuations while tending towards a decrease. The defective plate does not have as clear temperature steps and on average had lower temperatures than the clean print, while the strains also had a lower average value along with large fluctuations, but still tended towards decreasing over time. The plot in Figure 5.7 shows a very large spike in the middle of the second step. Based on these patterns, it

can be determined that a large increase or decrease in temperature or strain can determine the same change in the other quantity. It can also be said that the large spikes in the measured quantities can indicate the presence of defects along with an approximation of when the defect occurred in the plate.

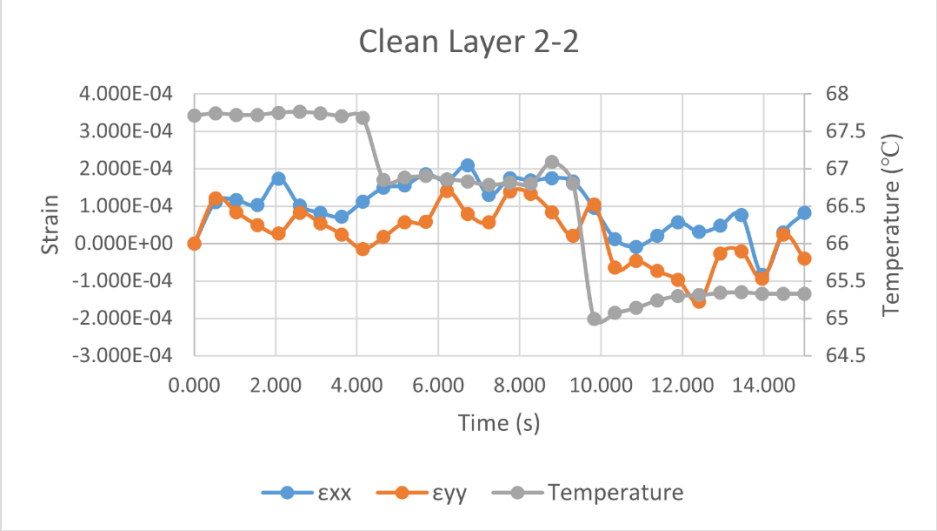

Figure 5.6 Plot of temperature and strains over time for the clean PLA print

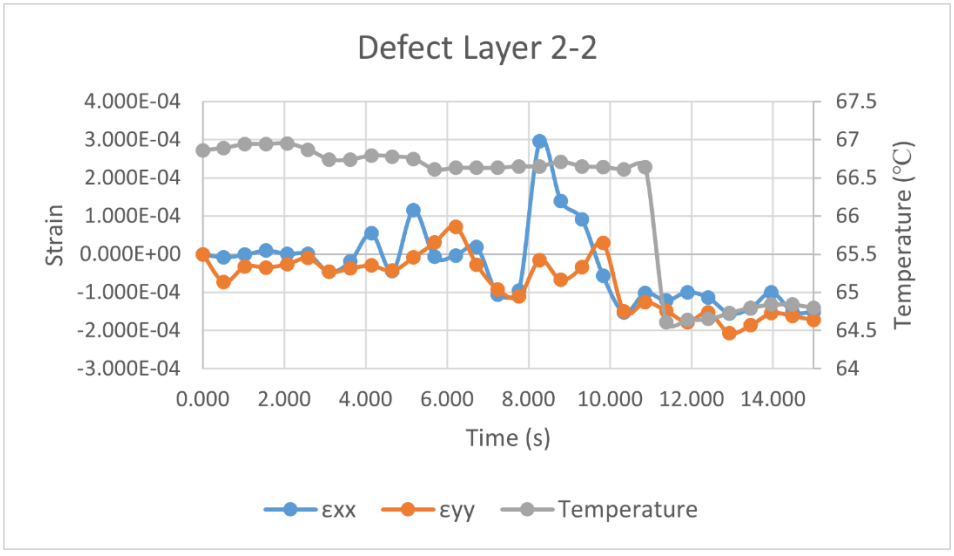

Figure 5.7 Plot of the temperatures and strain over time for the defect PLA print

5.3 Onyx Results

The Onyx testing starts using the baseline relations between heat, strain, and defect occurrences. The Onyx material also is not available in a speckled pattern version and there is no safe way to introduce speckles to the material without risking damage to the printer, so the DIC measurements could not be performed. In place of the DIC test, the ZBDNN was used to analyze pictures of clean and defective images to identify damage in the samples. This was done using images captured from the thermal camera, a grayscale CCD camera, and a combination of both. Defects were created using thin copper squares inserted under the painter's tape base the samples were printed on (pictured in Figure 5.8) or having the bed slightly lowered from the ideal location.

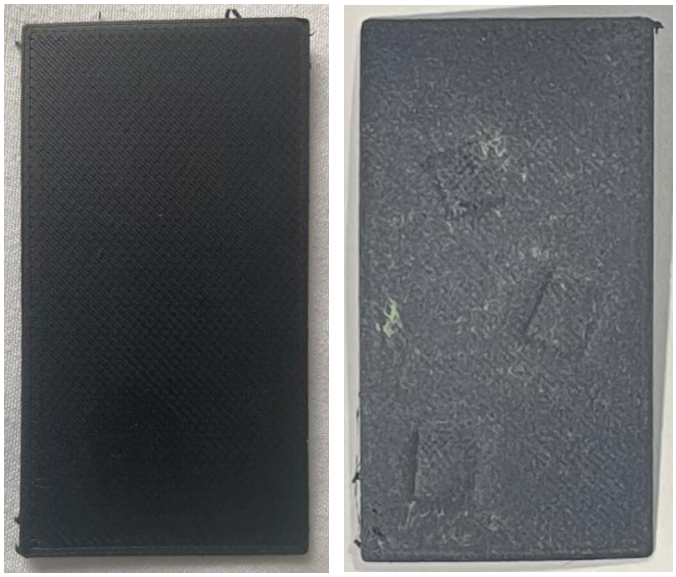

Figure 5.8 Samples of the clean Onyx prints (left) and the defect Onyx prints (right)

5.3.1 Thermal Results

This section discusses the results of the thermal data collected of the onyx samples for both the clean and the defective samples. The data discussed here was collected prior to the CCD images while the thermal data used in the combined test was collected with the CCD images.

5.3.1.1 Clean Prints

The Onyx composites were printed in an alternating 45°/-45° pattern which gave the thermal mappings of the layers distinctive patterns depending on which orientation they were printed in. The 45° layers, which are also the odd numbered layers, displayed a more rounded shape for each of the color gradients in the mapping, while the even-numbered -45° layers had a more flattened and elongated shape for the color gradients, as shown in Figure 5.9. In both cases, the cooling patterns were uniform, showing a gradual expansion of the gradients without any distortions to the shape indicating no defects present in the part.

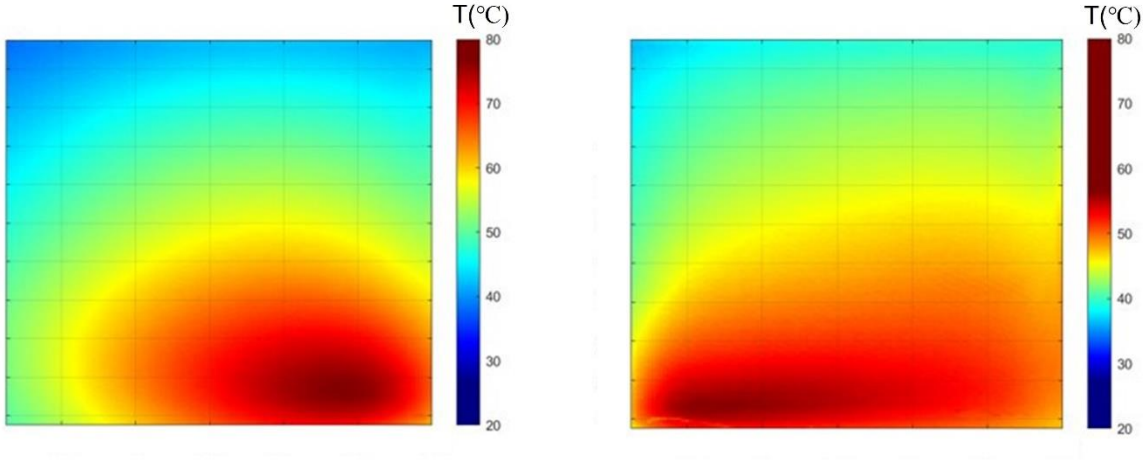

Figure 5.9 Thermal maps of the clean Onyx print at different layers

Plotting the average temperature in the sample shows a similar cooling pattern pictured in Figure 5.6 for the PLA prints. However, the step in the third layer is elevated due to the automatic increased heating of the Mark Two printer nozzle that accounts for the temperature difference between layers. Given the steps for layer 2 and layer 3 are even, it can be safely determined that step 3 would have had a decrease like that from the PLA samples.

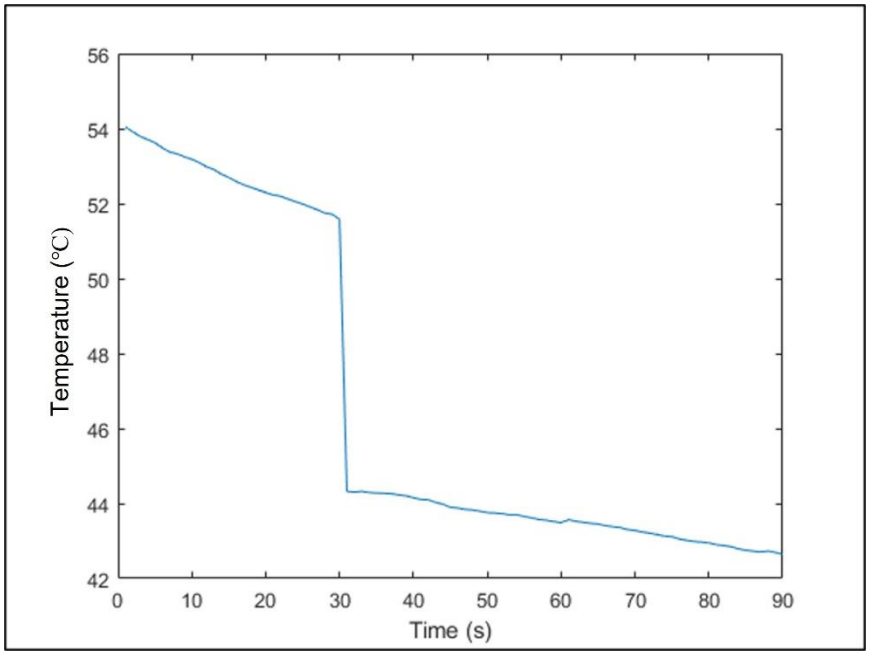

Figure 5.10 Plot of average temperature of the clean Onyx plate over time

5.3.1.2 Defective Prints

The defective set of prints displayed similar color gradients to that of the clean samples, however, they had clear distortions of colder regions in the shape of the copper squares which the gradients wrapped around as seen in Figure 5.11. For better visualization, image subtraction was performed by subtracting the color map of a clean image from an image of a defect at the same time step. The defect regions stand out much clearer as yellow in Figure 5.12.

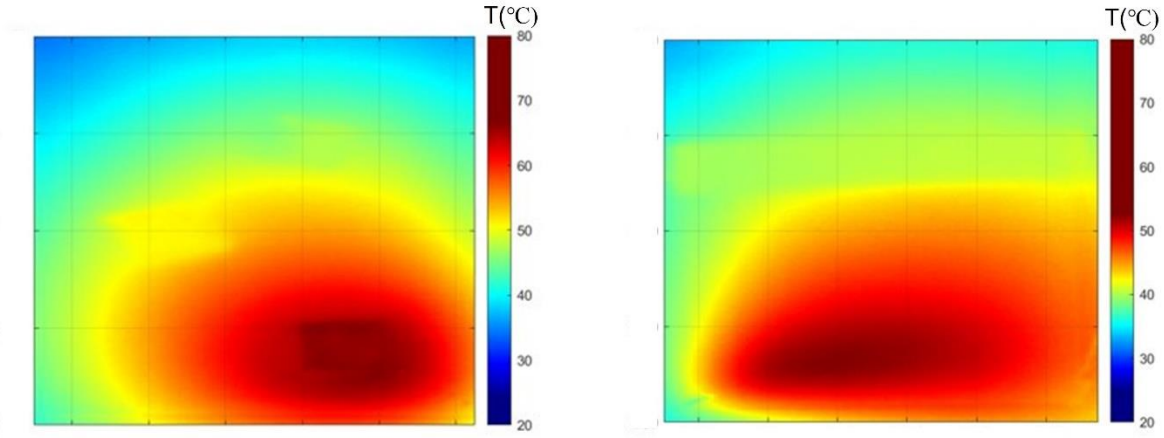

Figure 5.11 Thermal maps of the defect Onyx print at different layers

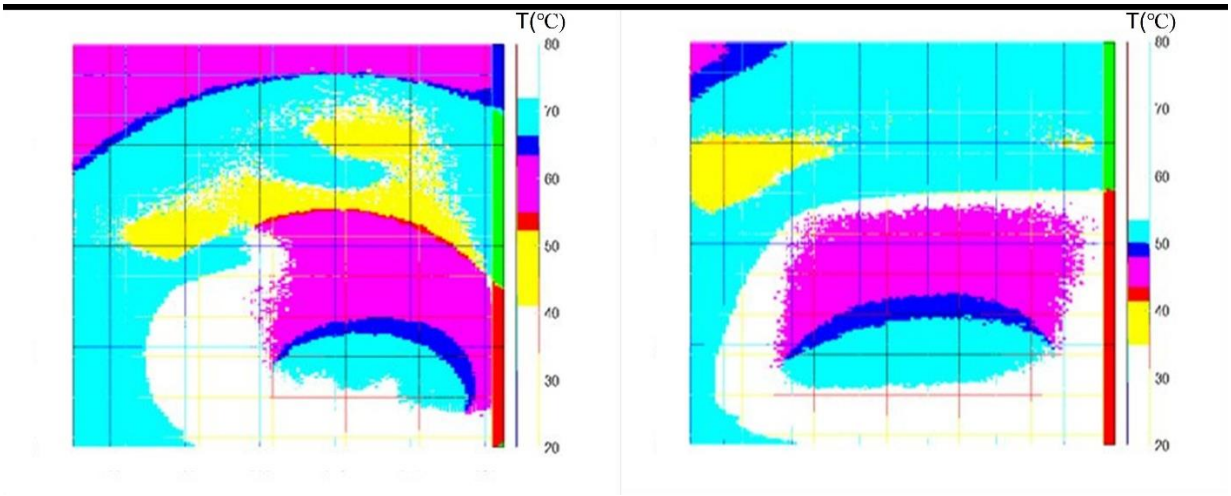

Figure 5.12 Subtraction of the clean and defect Onyx print thermal maps

The plot of the average temperature in Figure 5.13 displays a similar shape to clean print, however there are larger differences in temperature between each layer step. The average temperature overall was also cooler than the clean plot.

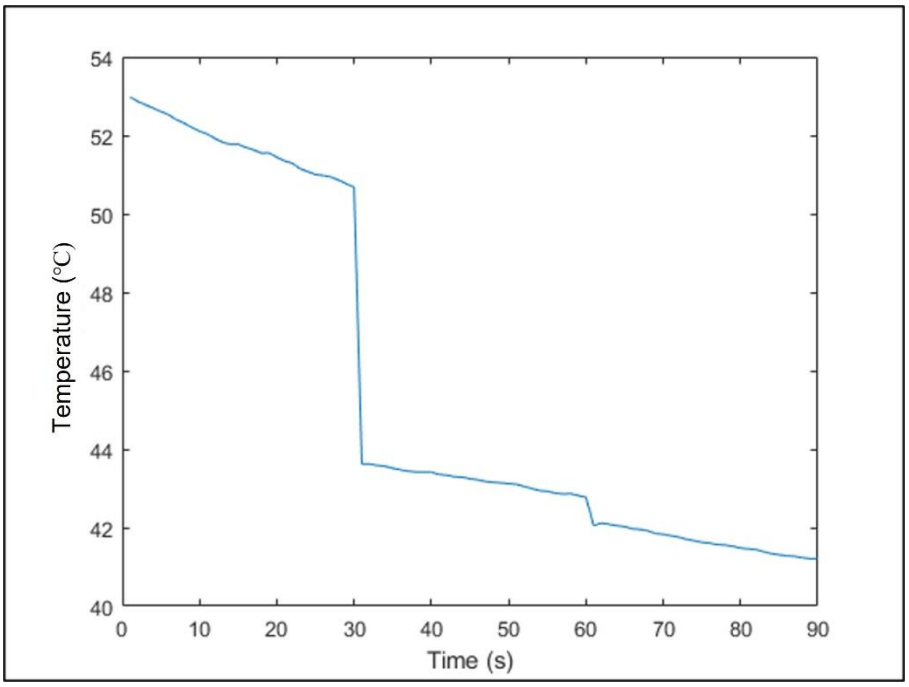

Figure 5.13 Plot of average temperature of the defect Onyx plate over time

6. Deep Neural Network Analysis

The ZBDNN was trained using the same images discussed previously to verify the results of the data. The training was done without the use of defective images so the program could learn what each layer is supposed to look like and anything that looks different enough could be caught and uniquely classified. The training results are given in Figure 6.1 and 6.2, with 6.1 showing the overall accuracy of the image classification and data loss and 6.2 showing a breakdown of how many images of each class were correctly and incorrectly identified. For this data, the program was 96.3% accurate with 5 images from layer 4 incorrectly classified as layer 1.

6.1 Thermal Results

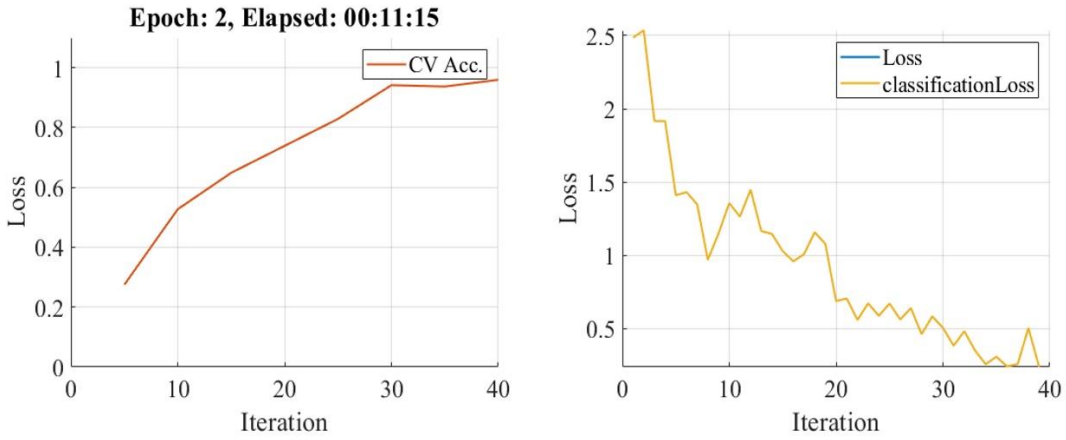

Figure 6.1 Accuracy and losses of the training data

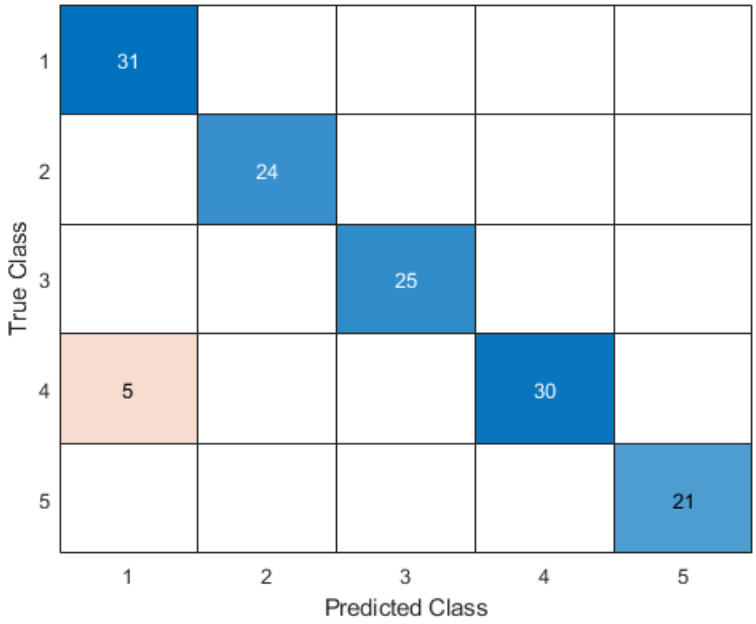

Figure 6.2 Class prediction of the training data

A Voronoi diagram was generated using the training data to better visualize the class data. This diagram breaks down a plane into smaller sections where similar data points are grouped into and separated from dissimilar data groupings. The data points in this experiment are the images and the sections are the layers of the plate. The diagram produced in Figure 6.3, while not perfect, displays that can be compared with a version that includes data points from defective images, shown in Figure 6.4, to determine if there is an issue with data analysis. Different sorting algorithms and distance metrics were observed and MATLAB's "exact" algorithm with the Spearman distance metric appeared to give the best sorting of the data.

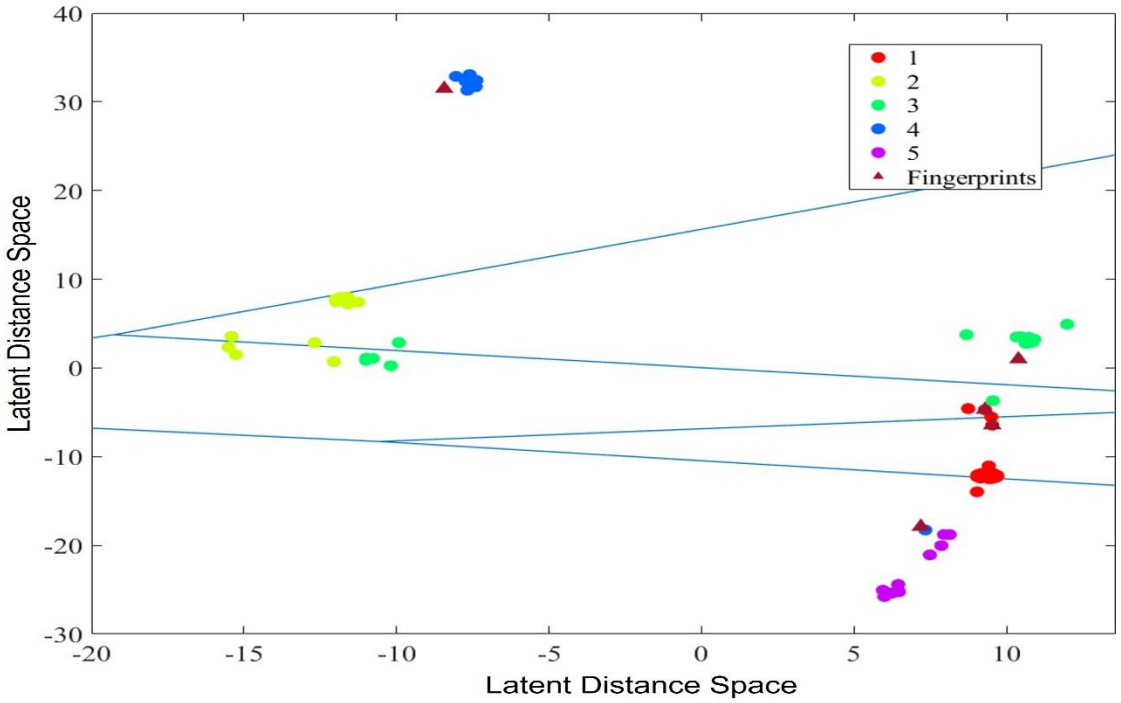

Figure 6.3 Voronoi diagram of ZBDNN results without images of defects

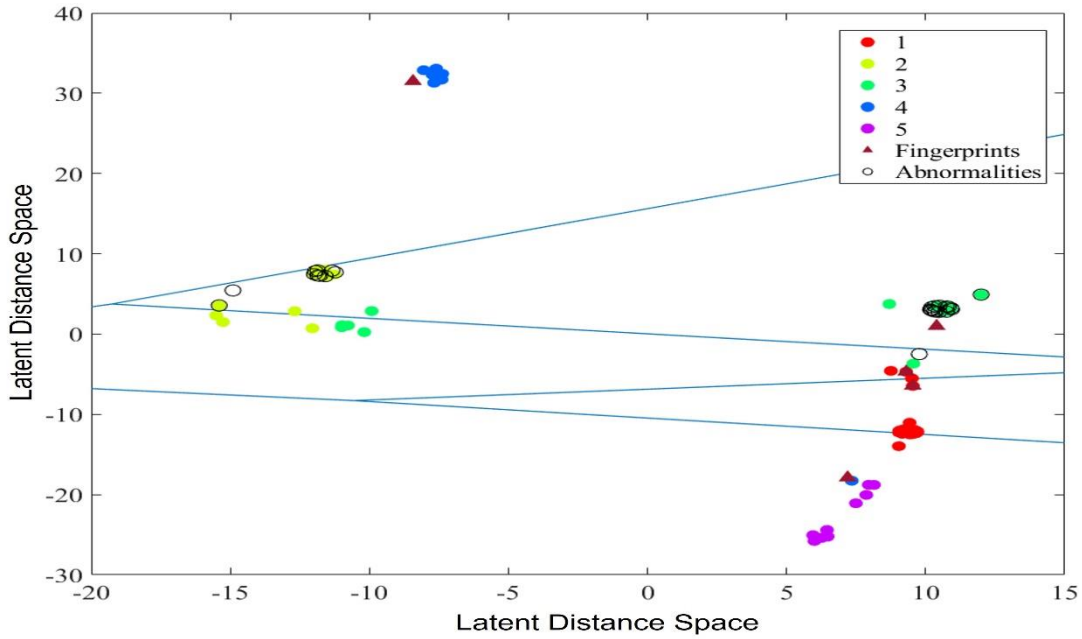

Figure 6.4 Voronoi diagram of ZBDNN results with images of defects

The patterns in this data include classes 2 and 3 being closely related along with classes 1 and 5 being closely related with some of class 1 spilling into class 5 with some of class 4. These patterns are seen in both Voronoi diagrams indicating that the analysis was accurate. It should also be noted that the data points visualized are clusters of smaller data points as shown in Figure 6.5. The data can be further verified by plotting flag data of positive and negative flags, including both true and false versions of each flag shown in Figure 6.6.

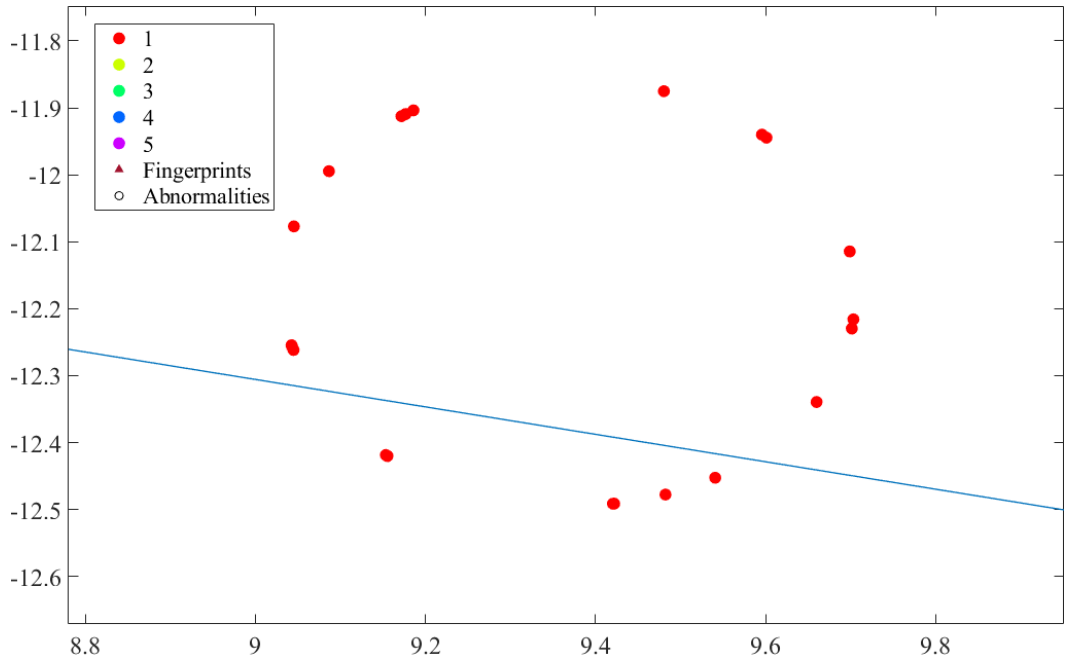

Figure 6.5 Zoom in of a "point" in class 1

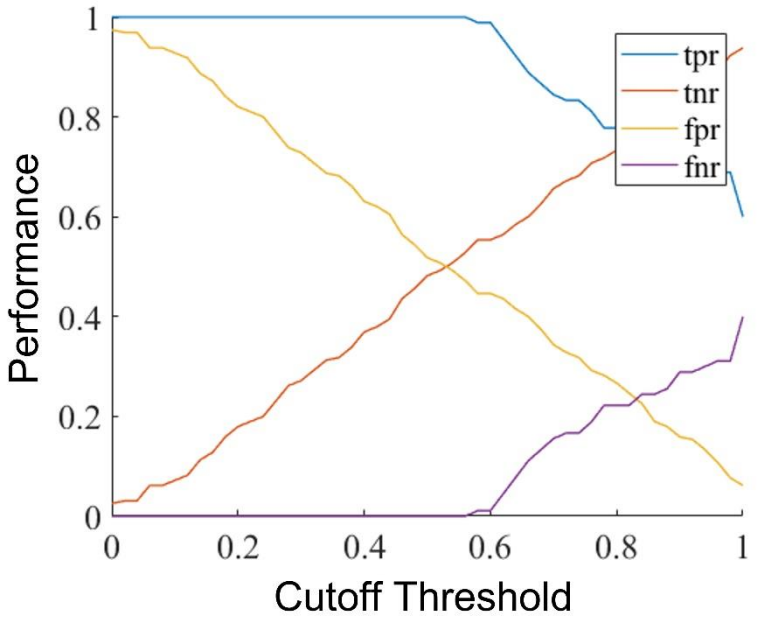

Figure 6.6 True and false positive and negative flags of the thermal images

6.2 CCD Results

Similar analysis was performed using grayscale images of plates. The analysis of these images was higher than that of the thermal images at 100% accuracy, although taking twice the number of iterations before the network concluded that the accuracy could not be improved further. A new set of thermal data was also captured in tandem with the grayscale images. Only 4 layers were used for this testing to reduce computation time of the combined analysis. The results of this testing had more distinctly separated classes albeit with some bleed over between classes as depicted in Figure 6.9 and Figure 6.10.

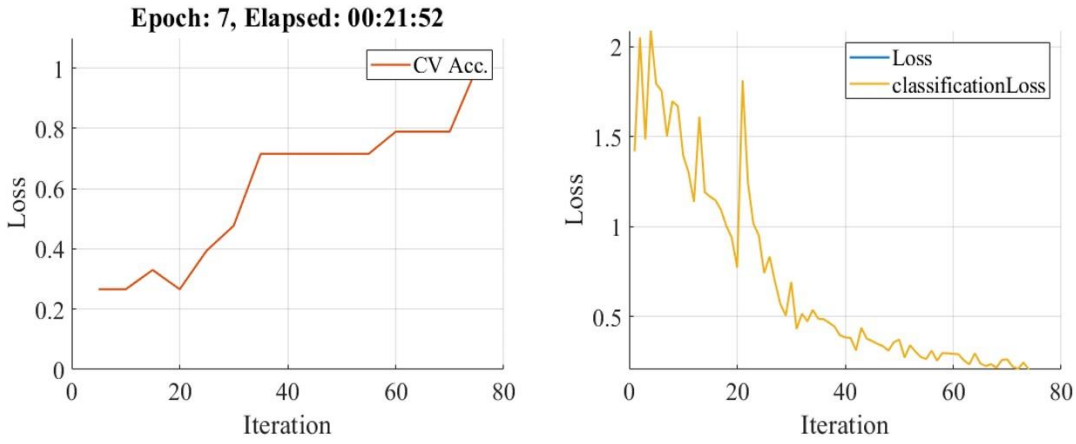

Figure 6.7 Accuracy and loss of the CCD photos

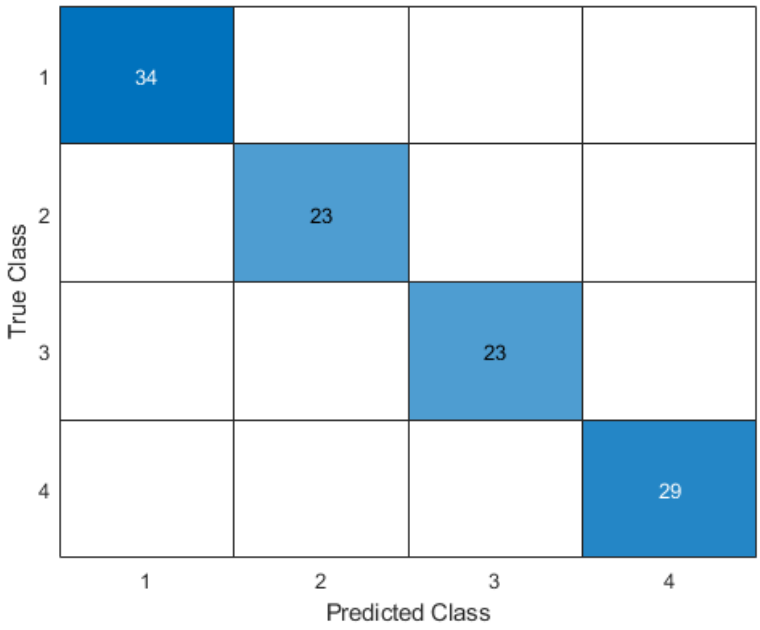

Figure 6.8 Class prediction of the CCD photos

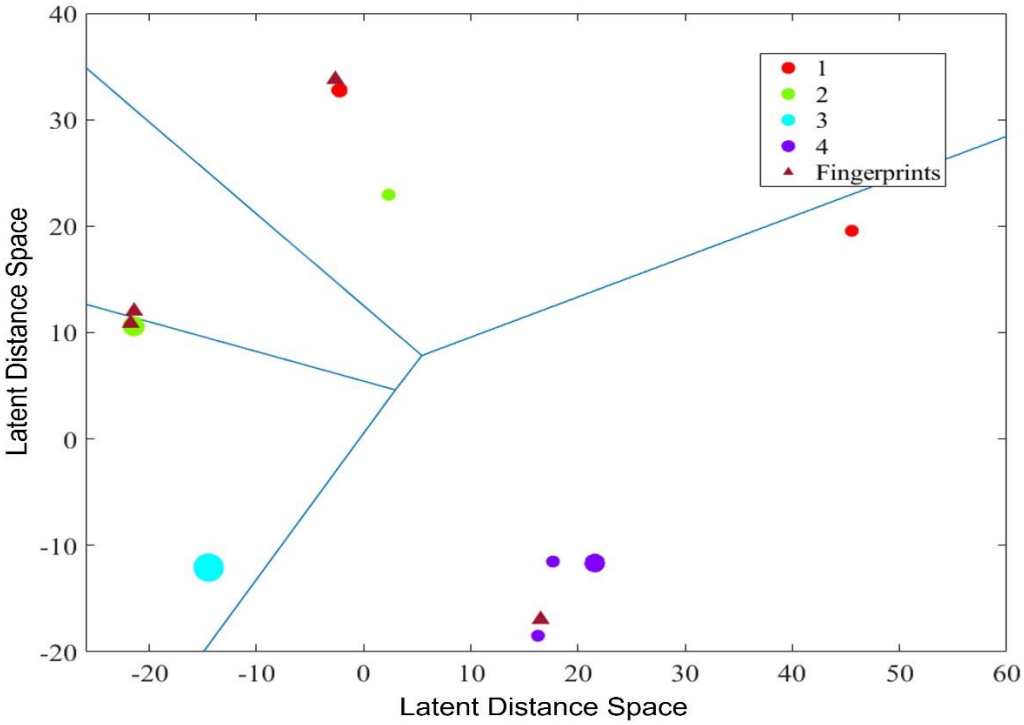

Figure 6.9 Voronoi of CCD images without defects

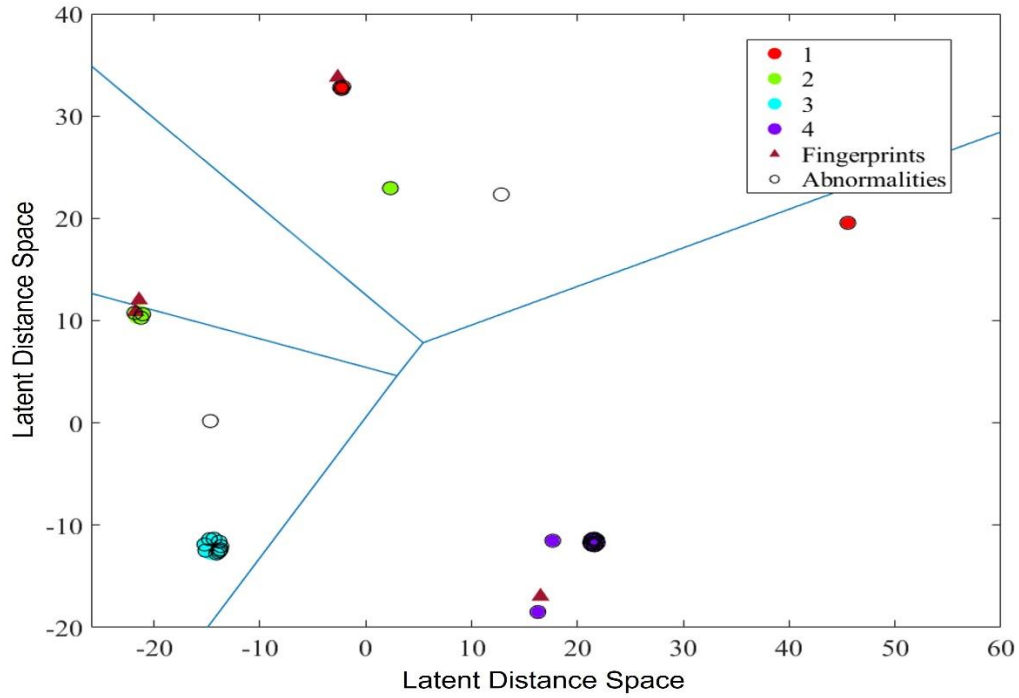

Figure 6.10 Voronoi of CCD images with defects

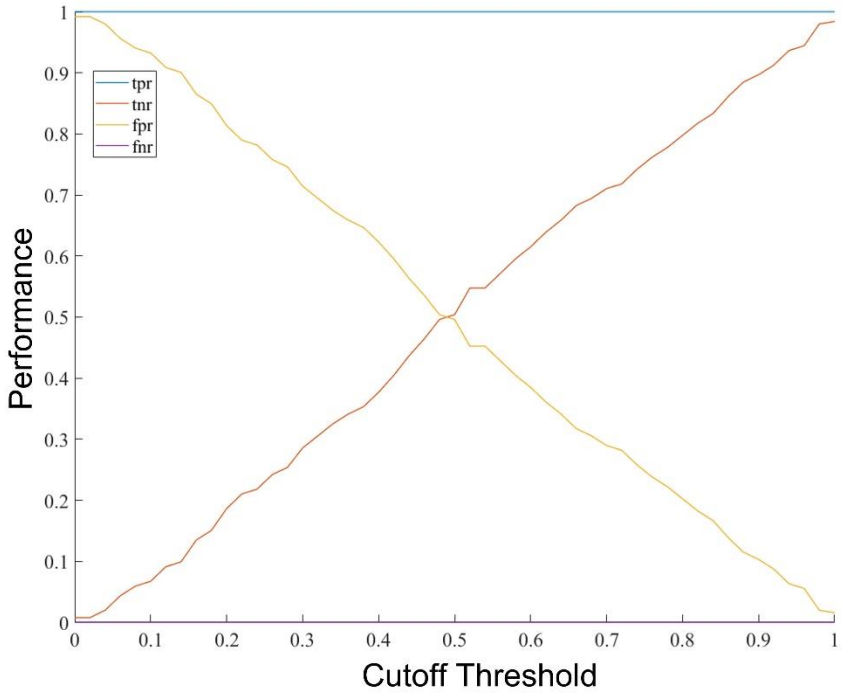

Figure 6.11 True and false positive and negative flags of the CCD images

6.3 Multiple Source Analysis

An analysis was also run combining the thermal data collected during the gray scale testing with the grayscale data. The thermal data encapsulates classes 1-4, and the grayscale data takes up classes 5-8. The thermal data was also converted into grayscale so that testing could be run as one of the matrices in the program had a value for color range, but grayscale images lacked this value. The testing would not run if only some of the data sets had ranges for this value but would if either all or none of the sets did. The accuracy of the combined testing was 98.6%, being slightly higher than the average between the two data sets, although taking more iterations either of the previous tests, before the network decided the accuracy couldn't be further improved.

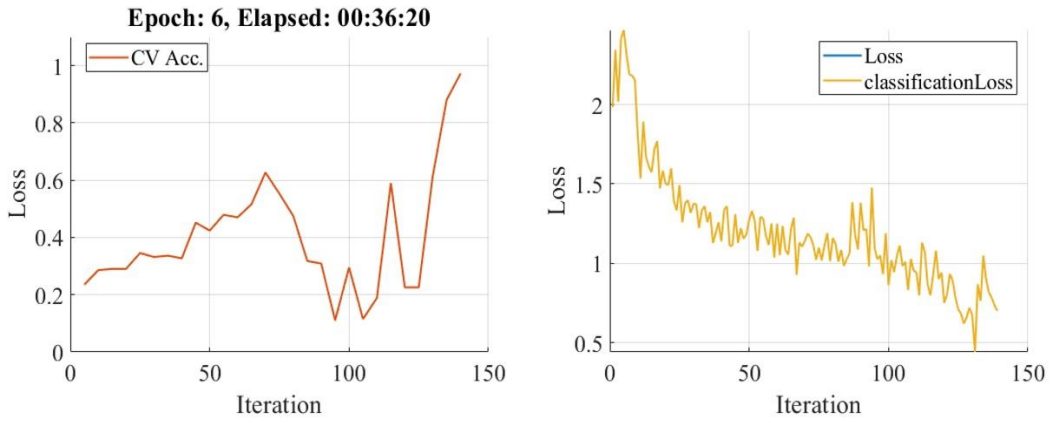

Figure 6.12 Accuracy and loss of the combined data

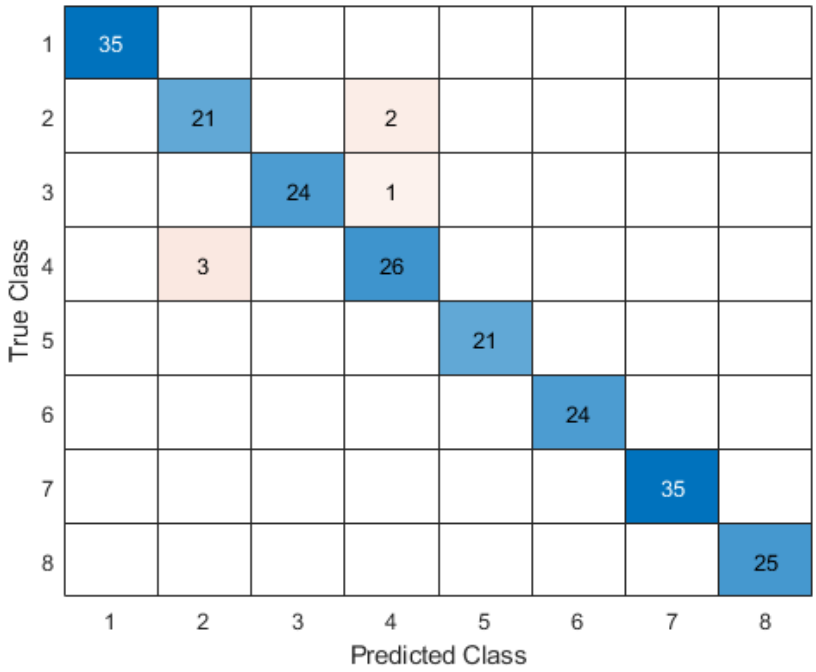

Figure 6.13 Class prediction of the combined data

The Voronoi of the combined data showed similar characteristics of both previous Voronoi diagrams, particularly with the layout of the defects. For the thermal data, most of the defects were detected around the 4th layer while the grayscale had most of the defects detected around

the 3rd layer. This indicates that even if one of the two methods is more accurate than the other, having both can be more beneficial when it comes to determining when defects are beginning to occur. For the thermal and grayscale, the even-numbered layers were closely related to each other and the odd-numbered layers shared this characteristic.

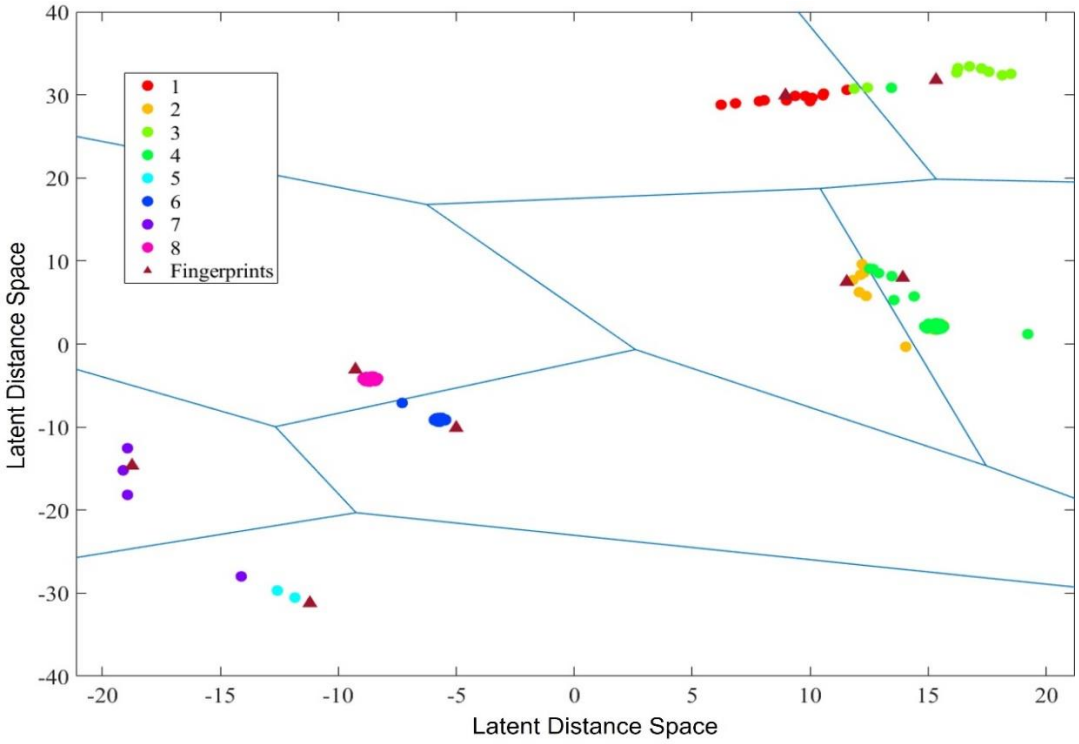

Figure 6.14 Voronoi of the combined test data without defects

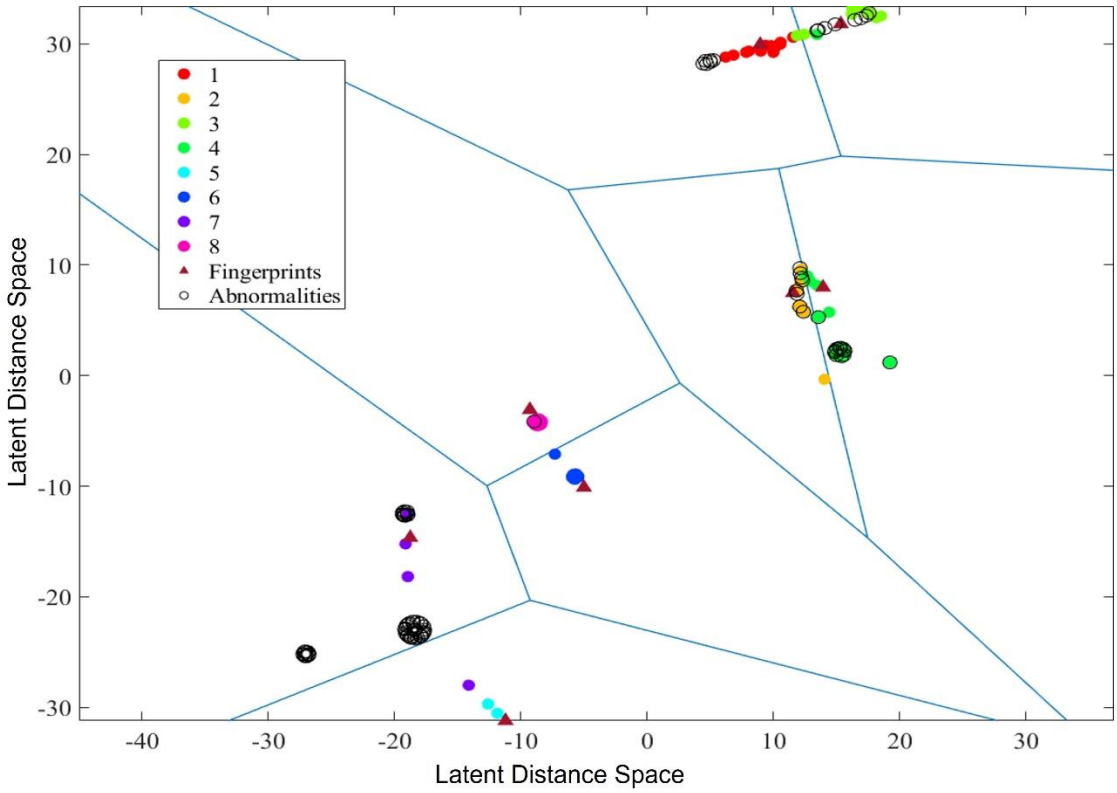

Figure 6.15 Voronoi of the combined test data with defects

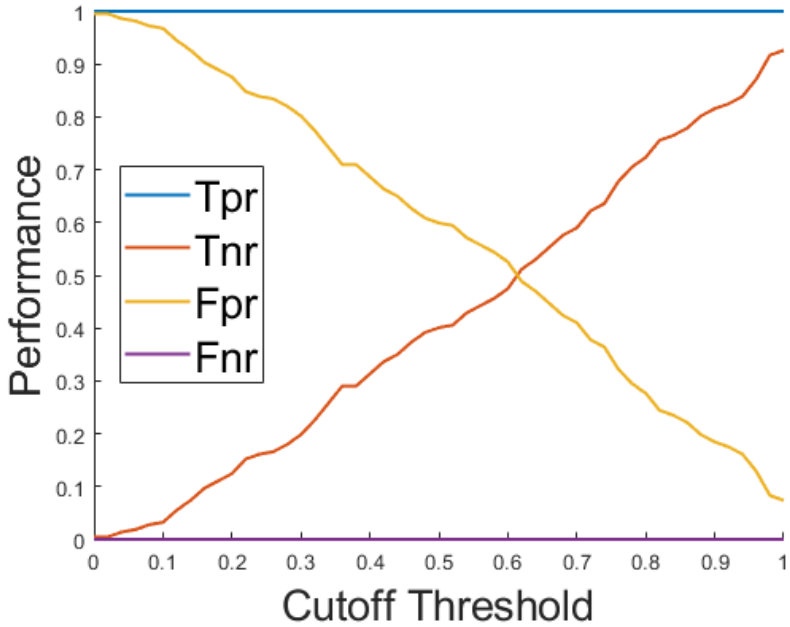

Figure 6.16 True and false positive and negative flags of the combined test data

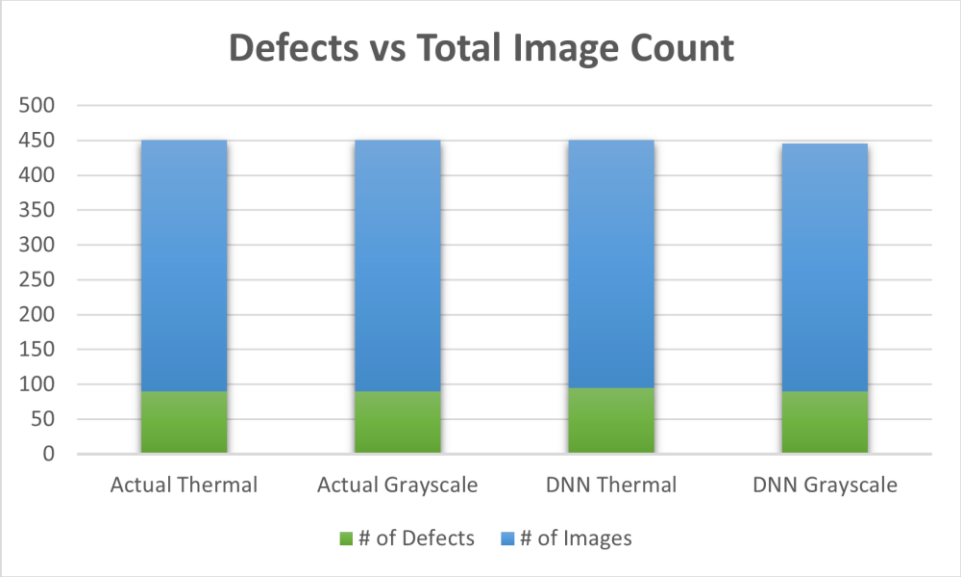

Figure 6.17 Comparing the total image count vs number of defect images for both data sets

7. Discussion

Using the PLA samples as a basis for developing correlations between strain and temperature and defect formations, any similarities found in the Onyx prints can be concluded to be the result of the FDM printing process. It was found that the strains in the defect samples tended to have wider ranges of strain values in both the xx and yy directions. It also had the largest fluctuations when the averages were plotted during the printing process. The thermal data collected showed the average temperature across the defective plates was lower than the clean samples by up to 5℃. There were also larger changes in temperature during different sections of printing which coincided with the appearance of strain spikes indicating a correlation between temperature and strain. These changes occurring only in the defect prints also show a correlation between these measured properties and the occurrences of defects. Testing of the Onyx samples displayed similar thermal patterns to the PLA samples indicating the patterns observed are primarily a result of the FDM printing method.

Expanding the data analysis of the Onyx samples to a zero-bias deep neural network, more details about the defect formations can be determined. Utilizing the thermal data as training data, the algorithm was able to properly classify the images by layer and defect occurrence 96.83% of the time. Plotting the data on a Voronoi indicates that most of the defects detected occurred in layer 2 and 3. The algorithm also closely plotted the even numbered layers with each other and the odd numbered layers with each other, likely due to the alternating 45°/-45° pattern in the print. Applying the same algorithm to a series of grayscale images taken at the same time and interval as the thermal images showed a similar, but different outcome. The algorithm was able to correctly classify the grayscale images 100% of the time. When plotting the data on a Voronoi diagram, the layers were clearly spaced apart, though the even and odd numbered layers did tend towards one

another like in the thermal case. The defects, however, were found on every layer, though primarily identified in layers 3 and 4 of the sample. The algorithm was also run utilizing both thermal and grayscale datasets at the same time. The algorithm was able to correctly classify the images 98.34% of the time, with the misclassifications occurring exclusively within the thermal images. Plotting the results on a Voronoi diagram showed similar patterns to the two individual test runs. The two sets were spaced apart in the diagram making them easy to identify. The sets still exhibited the clustering of even and odd number layers in the same fashion as they did individually. The defects were also similarly displayed in the grayscale set as they were in the individual tests except with the defects primarily being detected in layer 3. The thermal set displayed some defects detected in all the layers but primarily layers 2 and 4.

The results of the DNN tests indicate the most likely time occurrences for when the defects occur, which can be cross-referenced with the results of the in-situ tests to determine what is happening in the part at the time of defect formation. The DNN results also show that having multiple sources of data acquisition from multiple angles can help better the detection of defects in the algorithm.

8. Conclusions and Future Work

In this research, defect formations in Onyx composite prints from FDM style additive manufacturing was observed during the printing process through in-situ methods. The thermal data collected displays notable differences in cooling patterns between clean and defective prints. The cooling patterns can be related to those found in PLA prints which further indicates strain formations in Onyx are also similar. The data collected from the in-situ observations can be further analyzed using a deep neural network to classify images based on the layer pictured in the image. The inclusion of a zero-bias layer can keep the image classification consistent and more accurate. The Voronoi diagrams generated from the DNN can help determine when defects start to occur within the print, even if they are not noticeable through standard visual observations. Combining observations from different types of cameras can also help further conclude the origin of a defect in a print. The conclusions of this thesis include:

1. FDM style printing produces similar defect patterns between material types.
2. Defects in the composite plates displayed overall lower temperatures and higher fluctuations in strain than non-defective prints, with average temperature variations as high as 5°C and average strain variations as high as $3x10^{-4}$ between clean and defective prints.
3. The novel zero-bias deep neural network can be used to accurately classify image sets based on print layer and defect occurrence.
4. It is possible to use multiple image sources in a single DNN analysis to help pinpoint defect locations provided the images sets are in the same format.

The objectives of this thesis, to develop in-situ monitoring methods for the FDM process of composite materials, correlate measured process parameters with defect occurrences, and utilize

the characterization data in computational approaches were all accomplished. It was also possible to get detailed analysis of defect occurances from the neural network.

8.1 Future Work

This research accomplished defect detection by combining multiple sources of input data into one deep neural network analysis using a novel zero-bias layer. This work can be used as a reference for future research into defect analysis in additive manufacturing. It may be possible to use the 2D analysis performed in this research as the basis for developing an analysis utilizing a 3D view of a given print. Different materials printed using FDM can be observed and compared with this research to further observe material vs process effects on defect occurrences. Other printing processes, such as Selective Laser Sintering, that are analyzed could be compared to the results of this research to observe the effects different processes have on defect occurrences.

REFERENCES

[1] ASTM Subcommittee: F42.91 “Additive manufacturing — General principles — Fundamentals and vocabulary”, Book of Standards Volume: 10.04, ASTM ISO/ASTM52900-21

[2] HUBS, “3D printing trend report 2022”, 2022, https://www.hubs.com/get/trends/

[3] Ruiz-Morales, J. C., Tarancón, A., Canales-Vázquez, J., Méndez-Ramos, J., Afonso, L., Acosta-Mora, P., Rueda, J., & Fernández González, R. “Three dimensional printing of components and functional devices for energy and environmental applications”. Energy & Environmental Science. (2017). 10. 846-859. 10.1039/c6ee03526d.

[4] Vafadar, Ana, Ferdinando Guzzomi, Alexander Rassau, and Kevin Hayward. "Advances in Metal Additive Manufacturing: A Review of Common Processes, Industrial Applications, and Current Challenges" *Applied Sciences* 11, no. 3:1213. 2021. https://doi.org/10.3390/app11031213

[5] Blakey-Milner, B., Gradl, P., Snedden, G., Brooks, M., Pitot, J., Lopez, E., Leary, M., Berto, F., and du Plessis, A. “Metal additive manufacturing in aerospace: A review”, Materials & Design, Volume 209, 2021, https://doi.org/10.1016/j.matdes.2021.110008.

[6] NASA Jet Propulsion Laboratory, “NASA's Perseverance Rover Bringing 3D-Printed Metal Parts to Mars”, Solar System, 2020, https://www.jpl.nasa.gov/news/nasas-perseverance-rover-bringing-3d-printed-metal-parts-to-mars

[7] Bryan, W., “Future Rocket Engines May Include Large-Scale 3D Printing”, NASA, 3-D Printing, 2020, https://www.nasa.gov/centers/marshall/news/releases/2020/future-rocket-engines-may-include-large-scale-3d-printing.html

[8] Aerospace America, “Making 3D-printed parts for Boeing 787s”, Engineering Notebook, 2018, https://aerospaceamerica.aiaa.org/departments/making-3d-printed-parts-for-boeing-787s/

[9] Englert, L., Czink, S., Dietrich, S., and Schulze, V. “How defects depend on geometry and scanning strategy in additively manufactured AlSi10Mg”, Journal of Materials Processing Technology, Volume 299, 2022, https://doi.org/10.1016/j.jmatprotec.2021.117331.

[10] Mostafaei, A., Zhao, C., He, Y., Ghiaasiaan, S. R., Shao, B. S. S., Shamsaei, N., Wu, Z., Kouraytem, N., Sun, T., Pauza, J., Gordon, J. V., Webler, B., Parab, N. D., Asherloo, M., Guo, Q., Chen, L., and Rollett, A. D. “Defects and anomalies in powder bed fusion metal additive manufacturing”, Current Opinion in Solid State and Materials Science, Volume 26, Issue 2, 2022, https://doi.org/10.1016/j.cossms.2021.100974.

[11] Karpenko, O., Oterkus, S., and Oterkus, E., “Investigating the influence of residual stresses on fatigue crack growth for additively manufactured titanium alloy Ti6Al4V by using peridynamics”, International Journal of Fatigue, Vol. 155, 2022, https://doi.org/10.1016/j.ijfatigue.2021.106624.

[12] Fernandes, R. R., Tamijani, A. Y., and Al-Haik, M., “Mechanical characterization of additively manufactured fiber-reinforced composites”, Aerospace Science and Technology, Vol. 113, 2021, https://doi.org/10.1016/j.ast.2021.106653.

[13] Carlota, V., All You Need to Know About PLA for 3D Printing, 2023

[14] Farah, S., Anderson, D. G., and Langer, R. “Physical and mechanical properties of PLA, and their functions in widespread applications — A comprehensive review”, Advanced Drug Delivery Reviews, Volume 107, 2016, Pages 367-392, https://doi.org/10.1016/j.addr.2016.06.012.

[15] Aly, N. “A review on utilization of textile composites in transportation towards sustainability”. IOP Conference Series: Materials Science and Engineering. 2017. 254. 042002. 10.1088/1757-899X/254/4/042002.

[16] Markforged, “Onyx™”, https://markforged.com/materials/plastics/onyx

[17] FLIR, “An Overview of Thermography for Mechanical Applications”, 2018, https://www.flir.com/support-center/training/thermography-training/webinars/an-overview-of-thermography-for-mechanical-applications/

[18] Wilson, J., Everett, S., Dubay, R., Parsa, S. S., and Tyler, M., “Spatial predictive control using a thermal camera as feedback”, Measurement, Vol. 109, pgs. 384-393, 2017, https://doi.org/10.1016/j.measurement.2017.05.071.

[19] Borish, M., Post, B. K., Roschli, A., Chesser, P. C., Love, L. J., Gaul, K. T., Sallas, M., and Tsiamis, N., “In-Situ Thermal Imaging for Single Layer Build Time Alteration in Large-Scale Polymer Additive Manufacturing”, Procedia Manufacturing, Vol. 34, 2019, https://doi.org/10.1016/j.promfg.2019.06.202

[20] Chen, F., Wang, E., Zhang, B., Zhang, L., and Meng, F. “Prediction of Fracture Damage of Sandstone Using Digital Image Correlation”. Applied Sciences. 2020. 10. 1280. 10.3390/app10041280.

[21] Spencer, R., Hassen, A. A., Baba, J., Lindahl, J., Love, L., Kunc, V., Babu, S., Vaidya, U., “An innovative digital image correlation technique for in-situ process monitoring of composite structures in large scale additive manufacturing”, Composite Structures, Vol. 276, 2021, https://doi.org/10.1016/j.compstruct.2021.114545.

[22] IBM, “What are neural networks?”, https://www.ibm.com/topics/neural-networks

[23] Wang, M., Cheung, S. W., Chung, E., Efendiev, Y., Leung, W., & Wang, Y. “Prediction of Discretization of GMsFEM Using Deep Learning”, Mathematics, 2019. 7. 412. 10.3390/math7050412.

[24] TURING, “What Is the Necessity of Bias in Neural Networks?”, https://www.turing.com/kb/necessity-of-bias-in-neural-networks#what-is-bias-in-a-neural-network?

[25] Liu, Y., Chen, Y., Wang, J., Niu, S., Liu D., and Song, H. "Zero-bias Deep Neural Network for Quickest RF Signal Surveillance," 2021 IEEE International Performance, Computing, and Communications Conference (IPCCC), Austin, TX, USA, 2021, pp. 1-8, doi: 10.1109/IPCCC51483.2021.9679426.

[26] Liu, Y., Wang, J., Li, J., Niu, S., Wu L., and Song, H. "Zero-Bias Deep-Learning-Enabled Quickest Abnormal Event Detection in IoT," in IEEE Internet of Things Journal, vol. 9, no. 13, pp. 11385-11395, July1, 2022, doi: 10.1109/JIOT.2021.3126819.

[27] Martina Jani, “IN-SITU MONITORING OF ADDITIVE MANUFACTURING USING DIGITAL IMAGE CORRELATION”, Embry-Riddle Aeronautical University, 2021

[28] Liu, Y., Wang, J., Li, J., Song, H., Yang, T., Niu, S., and Ming, Z. "Zero-Bias Deep Learning for Accurate Identification of Internet-of-Things (IoT) Devices," in IEEE Internet of Things Journal, vol. 8, no. 4, pp. 2627-2634, Feb. 15, 2021, doi: 10.1109/JIOT.2020.3018677.

[29] Liu, Y., Wang, J., Li, J., Niu S., and Song, H. "Class-Incremental Learning for Wireless Device Identification in IoT," in IEEE Internet of Things Journal, vol. 8, no. 23, pp. 17227-17235, Dec. 1, 2021, doi: 10.1109/JIOT.2021.3078407.